

# Hominins on Sulawesi during the Early Pleistocene

<https://doi.org/10.1038/s41586-025-09348-6>

Received: 14 May 2024

Accepted: 1 July 2025

Published online: 6 August 2025

Open access

 Check for updates

Budianto Hakim<sup>1,2✉</sup>, Unggul Prasetyo Wibowo<sup>3</sup>, Gerrit D. van den Bergh<sup>4</sup>, Dida Yurnaldi<sup>5</sup>, Renaud Joannes-Boyau<sup>6</sup>, Akin Duli<sup>2,7</sup>, Suryatman<sup>2,7</sup>, Ratno Sardi<sup>1,2</sup>, Indah Asikin Nurani<sup>1</sup>, Mika Rizki Puspaningrum<sup>8</sup>, Irfan Mahmud<sup>1,2</sup>, Afdalah Haris<sup>9</sup>, Khairun Al Anshari<sup>9</sup>, Andi Muhammad Saiful<sup>2,7</sup>, P. Arman Bungaran<sup>9</sup>, Shinatria Adhityatama<sup>10,11</sup>, Putra Hudlinas Muhammad<sup>9</sup>, Anwar Akib<sup>12</sup>, Nani Somba<sup>13</sup>, Fakhri<sup>14</sup>, Basran Burhan<sup>10</sup>, Zubair Mas'ud<sup>1,2</sup>, Mark W. Moore<sup>15</sup>, Yinika L. Perston<sup>10,11</sup>, Wenjing Yu<sup>6</sup>, Maxime Aubert<sup>6,11</sup> & Adam Brumm<sup>10,16✉</sup>

The dispersal of archaic hominins beyond mainland Southeast Asia (Sunda)<sup>1</sup> represents the earliest evidence for humans crossing ocean barriers to reach isolated landmasses<sup>2–4</sup>. Previously, the oldest indication of hominins in Wallacea, the oceanic island zone east of Sunda, comprised flaked stone artefacts deposited at least  $1.02 \pm 0.02$  million years ago (Ma) at Wolo Sege on Flores<sup>5</sup>. Early hominins were also established on the oceanic island of Luzon (Philippines), as indicated by both stone artefacts and cut marks on faunal remains dating to between 777 and 631 thousand years ago (ka) at Kalinga<sup>6</sup>. Moreover, fossils of extinct, small-bodied hominins occur on Flores (*Homo floresiensis*)<sup>7–12</sup> and Luzon (*Homo luzonensis*)<sup>13</sup>. On Sulawesi, the largest Wallacean island, previous excavations revealed stone artefacts with a minimum age of 194 ka at the open site of Talepu in the Walanae Depression<sup>14</sup>, long preceding the earliest known presence of modern humans (*Homo sapiens*) in the region (73–63 ka in Sunda)<sup>15</sup>. Here we show that stone artefacts also occur at the nearby site of Calio in fossiliferous layers dated to at least 1.04 Ma and possibly up to 1.48 Ma, using palaeomagnetic dating of sedimentary rocks and coupled Uranium-series (U-series) and electron-spin resonance (US–ESR) dating of fossil teeth. The discovery of Early Pleistocene artefacts at Calio suggests that Sulawesi was populated by hominins at around the same time as Flores, if not earlier.

The Indonesian island of Sulawesi was formed by the collision of the Eurasian Plate, the Indo-Australian Plate and the Pacific Plate<sup>16</sup>. In the island's southwestern peninsula, this complex tectonic history resulted in the formation, during the Miocene, of an elongate north-to-south trending basin (the Walanae Depression) that is bounded on both sides by a major fault system oriented in the same direction, the Walanae Fault Zone<sup>17</sup>. Around the Pliocene–Pleistocene transition, the basin extension reversed to an east–west compressional regime that led to basin inversion<sup>18</sup>. The Sengkang Anticline forms the surface expression of a reverse fault<sup>17,19</sup> generated during this phase (Extended Data Fig. 1). The regressive basin infill sequence, the Walanae Formation, is 1,800 m thick as exposed in the Sengkang Anticline<sup>19</sup>.

The uppermost stratigraphic unit of the Walanae Formation is the deltaic Beru Member (modern Indonesian spelling Berru), which is

characterized by an alternation of water-laid sandstones, conglomerates and silty-clay deposits<sup>14,19</sup>. The Beru Member has been further subdivided into a lower Sub-Unit A, which is dominated by fine-grained lagoonal and fluviodeltaic clastic deposits, and an upper Sub-Unit B, characterized by coarse-grained fluvial and estuarine clastic deposits<sup>14,19</sup>. Vertebrate fossils occur primarily in the coarse-grained sedimentary layers of the Beru Member, but have also been found in fine-grained floodplain and estuarine deposits<sup>14,19</sup>. The fossil beds of Sub-Unit A are estimated to be Late Pliocene to Early Pleistocene in age, whereas an 18-m-thick sequence pertaining to the younger Sub-Unit B, outcropping near Talepu, ranges from about 100 ka near the top to at least 194 ka towards the base<sup>14</sup>. Fossils of extinct fauna occur right at the bottom of Sub-Unit A (defined as the first fluvial sandstone layer), including elements attributed to a large suid, *Celebochoerus heekereni*, and small-bodied proboscideans<sup>19</sup>.

<sup>1</sup>Pusat Riset Arkeologi Prasejarah dan Sejarah (Badan Riset dan Inovasi Nasional (BRIN)), Jakarta, Indonesia. <sup>2</sup>Pusat Kolaborasi Riset Arkeologi Sulawesi (BRIN–Universitas Hasanuddin), Makassar, Indonesia. <sup>3</sup>Museum Geologi Bandung, Bandung, Indonesia. <sup>4</sup>Environmental Futures, University of Wollongong, Wollongong, New South Wales, Australia. <sup>5</sup>Centre for Geological Survey, Geological Agency of Indonesia, Bandung, Indonesia. <sup>6</sup>Geoarchaeology and Archaeometry Research Group, Southern Cross University, Lismore, New South Wales, Australia. <sup>7</sup>Departemen Arkeologi, Universitas Hasanuddin, Makassar, Indonesia. <sup>8</sup>Faculty of Earth Sciences and Technology, Bandung Institute of Technology, Bandung, Indonesia. <sup>9</sup>Indonesian Association of Archaeologists (IAAI Komda Sulawesi), <https://iaai.or.id/>. <sup>10</sup>Australian Research Centre for Human Evolution, Griffith University, Brisbane, Queensland, Australia. <sup>11</sup>Griffith Centre for Social and Cultural Research, Griffith University, Gold Coast, Queensland, Australia. <sup>12</sup>Pemerhati dan Pelestari Budaya di Soppeng, Soppeng, Indonesia. <sup>13</sup>Pusat Riset Arkeologi Lingkungan, Maritim dan Budaya Berkelanjutan (BRIN), Jakarta, Indonesia. <sup>14</sup>Pusat Riset Arkeometri (BRIN), Makassar, Indonesia. <sup>15</sup>Archaeology and Palaeoanthropology, University of New England, Armidale, New South Wales, Australia. <sup>16</sup>School of Environment and Science, Griffith University, Brisbane, Queensland, Australia. <sup>✉</sup>e-mail: [budi060@brin.go.id](mailto:budi060@brin.go.id); [a.brumm@griffith.edu.au](mailto:a.brumm@griffith.edu.au)

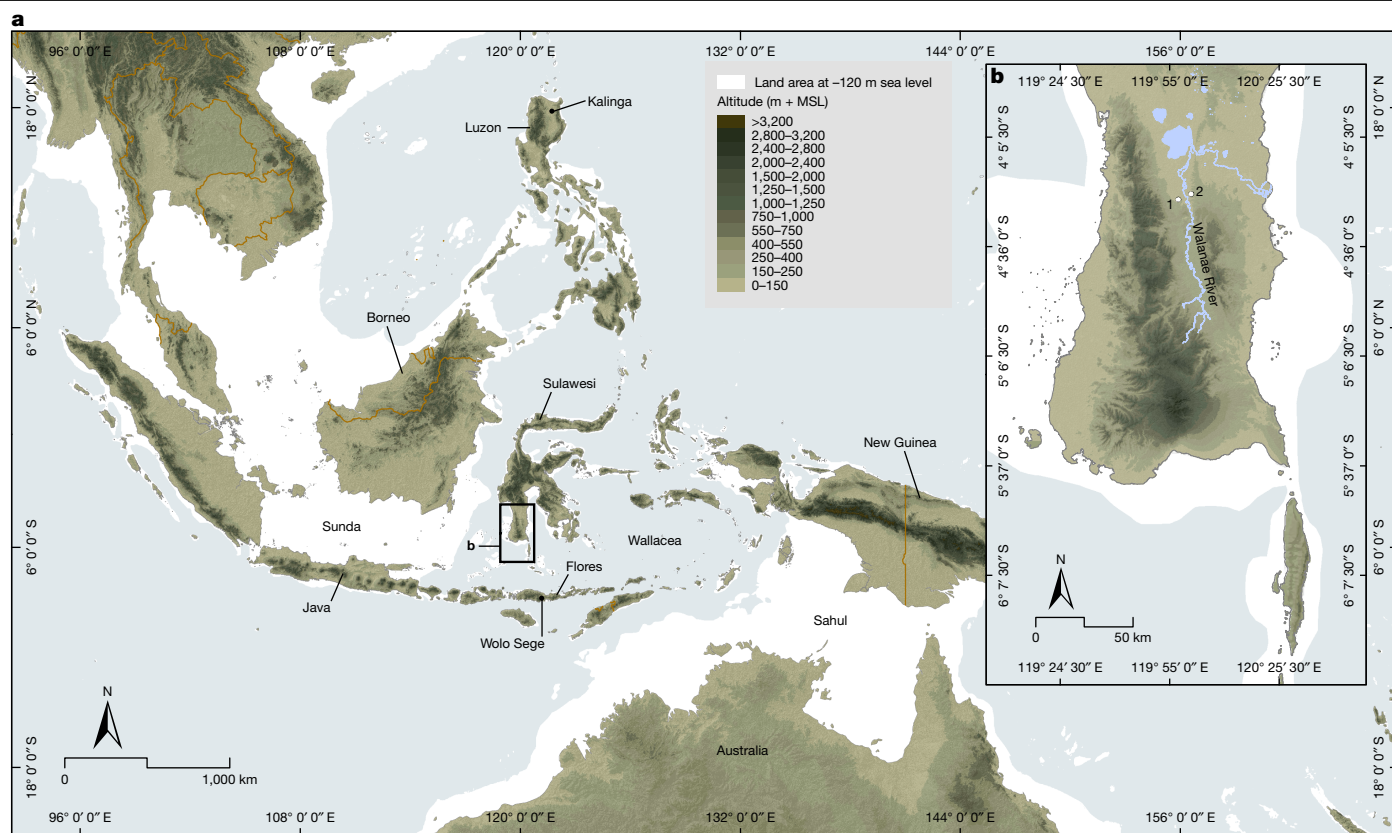


**Fig. 1 | Map of the study area. a**, The location of Sulawesi within the Wallacean archipelago (Wallacea)—the zone of oceanic islands between the Asian and Australian continental regions (Sunda and Sahul, respectively). MSL, mean sea level. **b**, The southwestern peninsula of Sulawesi, showing the locations of the

Talepu (1) and Calio (2) sites on opposite sides of the Walanae River. Sources of map data: General bathymetric maps ([https://www.gebco.net/data\\_and\\_products/gridded\\_bathymetry\\_data/](https://www.gebco.net/data_and_products/gridded_bathymetry_data/)); DEMNAS Badan Informasi Geospasial (<https://tanahair.indonesia.go.id/demnas/#/demnas>).

Calio (4° 20' 8" S, 120° 00' 48.3" E) is located at 57 m above sea level near the village of Ujung (Lilirilau district) in the Soppeng Regency (Fig. 1 and Extended Data Figs. 1 and 2). It is situated some 2.3 km east of the Walanae River and around 36 m above its active floodplain. A series of fluvial pebbly sandstones belonging to the Beru Member Sub-Unit B of the Walanae Formation is exposed at the ground surface at this site over an area of about 63,000 m<sup>2</sup>. Previous studies had interpreted these subhorizontally bedded, coarse-grained fluvial deposits as ancient river terraces of the Walanae River<sup>20–22</sup>, with the earliest of these 'terrace fills' deemed to be at most 50 ka (ref. 22). However, subsequent work has revealed that exposures of these strata adjacent to the Walanae River near Calio represent the uplifted upper part of the regressive basin-fill sequence (Beru Member Sub-Unit B of the Walanae Formation)<sup>14,19</sup>. Sub-Unit A of the Beru Member is better exposed further to the east in the west-dipping west flank of the Sengkang Anticline<sup>19</sup>. The Beru Member Sub-Unit B deposits had long been associated with surface-collected lithic artefacts recovered from the same area<sup>21</sup>. However, it was not until 2016 that culturally modified stones were shown conclusively to be present in situ within these fluvial layers, with the earliest lithic artefacts dating to at least 194 ka at Talepu<sup>14</sup>.

The Calio site first drew attention when a stone artefact (a chert flake denoted artefact 1) was found embedded in a heavily cemented conglomerate with subhorizontal bedding plane exposed on the ground surface in an agricultural field (Fig. 2a and Extended Data Fig. 3g). Systematic excavations were carried out in these Beru Member Sub-Unit B deposits in 2019 and 2021–2022 (Extended Data Fig. 2), targeting an area on an east-northeast–west-southwest trending ridge. In 2019, we opened a total of six contiguous 1 m<sup>2</sup> excavation units (denoted squares B1U1 to B1U6) using arbitrary 10-cm-thick intervals (spits)

(Fig. 3 and Extended Data Fig. 3a). The first square, B1U1, was initiated at the find site of artefact 1. An additional nine 1 m<sup>2</sup> units (B2U1 to B2U3, B3U1–B3U3 and B4U1–B4U3) were placed on the west side of the previously excavated units in 2021–2022. These excavations revealed an up to 1.4-m-thick sequence of fluvial deposits (Fig. 3 and Extended Data Figs. 2e and 3a,b) consisting of crudely bedded, poorly sorted and coarse pebbly sandstone, capped by a layer of extremely hard, 15–25-cm-thick conglomerate that had been cemented by calcium carbonate (layer 2). The coarse clastic deposits consist primarily of weathered volcanic rock fragments, but also contain chert/silicified limestone pebbles and siltstone and claystone rip clasts, whereas the fine-grained sandy fraction consists of volcanic rock fragments and minor feldspar, quartz and pyroxene crystals. Pebbles and grains are subangular to rounded. Layer 2 has an average clast diameter of granule size with a few larger pebbles with a maximum diameter of around 30 mm. A *Celebochoerus* maxilla with dentition (Fig. 3 (F1)) was excavated 30 cm below the ground surface at the bottom of this very coarse sandstone (square B1U1) (Extended Data Fig. 4). The fossilized bone tissue of the maxilla is poorly preserved and partly dissolved; however, the worn molars in the left and right tooth rows are in excellent condition, exhibiting no signs of fluvial wear, suggesting that this particular fossil was not reworked from older strata. Aside from this isolated suid element, remains of terrestrial mammals comprised a tooth fragment from a juvenile proboscidean recovered from square B3U1 at a depth of 30–40 cm. Other excavated fossil fauna included a crocodile tooth and several teeth of small-sized sharks (possibly reworked or brackish/freshwater species). A small number of indeterminate waterworn fossil bone fragments was also found dispersed throughout the deposit, as were irregular discontinuous carbonate concretions.



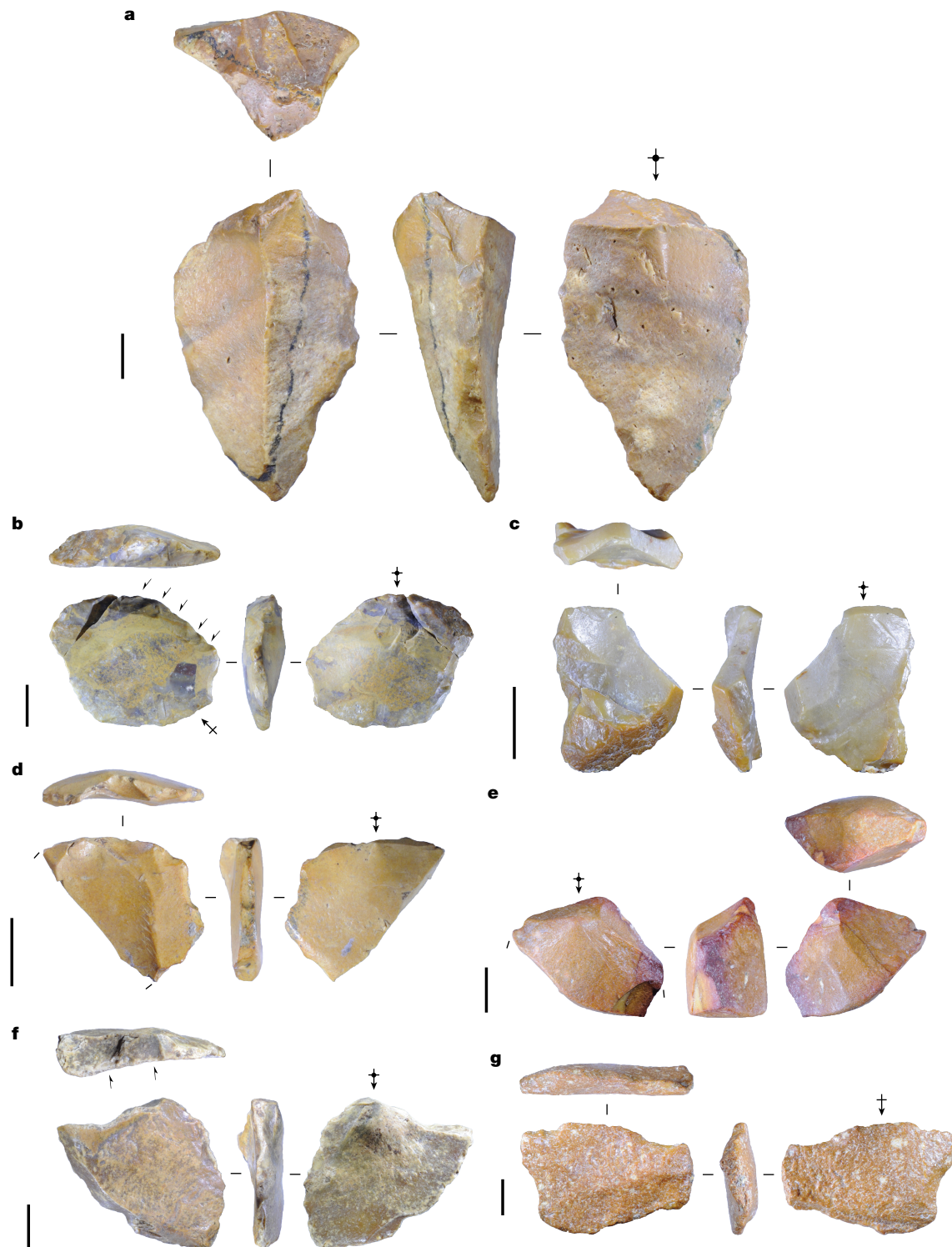


**Fig. 2 | Stone artefacts recovered from Early Pleistocene deposits at Calio.**

**a**, Artefact 1: a large chert flake discovered partially exposed on the surface in a heavily cemented conglomerate. A black linear mineral stain marks the boundary between the exposed part of the flake and the portion embedded in the sandstone. **b**, Artefact 2: a medium-sized retouched flake struck from a core made from brecciated chert. The arrows indicate the direction of retouch scars across the dorsal face. **c**, Artefact 3: a small flake struck from a water-rolled

chert cobble. **d**, Artefact 4: a small flake with moderate taphonomic (that is, non-cultural) flaking to both faces (it is broken diagonally). **e**, Artefact 5: the proximal end of a large flake broken by weathering. **f**, Artefact 6: a medium-sized redirecting flake struck onto a relatively flat cortical surface of a water-worn chert cobble. **g**, Artefact 7: a heavily abraded flake with moderate to heavy taphonomic flaking to both faces. Scale bars, 10 mm.

In total, seven flaked stone artefacts (Fig. 3 (A1–A7)) were recovered in situ within the Beru Member Sub-Unit B sandstone at Calio (Fig. 2a–g, Extended Data Figs. 2e and 3c–f and Supplementary Information). The artefacts were found at different depths and in two distinct sedimentary

layers (layers 2 and 3b; Fig. 3). As noted above, one artefact (artefact 1) was embedded in the hardened cap layer (layer 2) at the modern ground surface in square B1U1 (Extended Data Fig. 3b,g). The stratigraphically lowest specimen (artefact 6) was recovered from layer 3b,

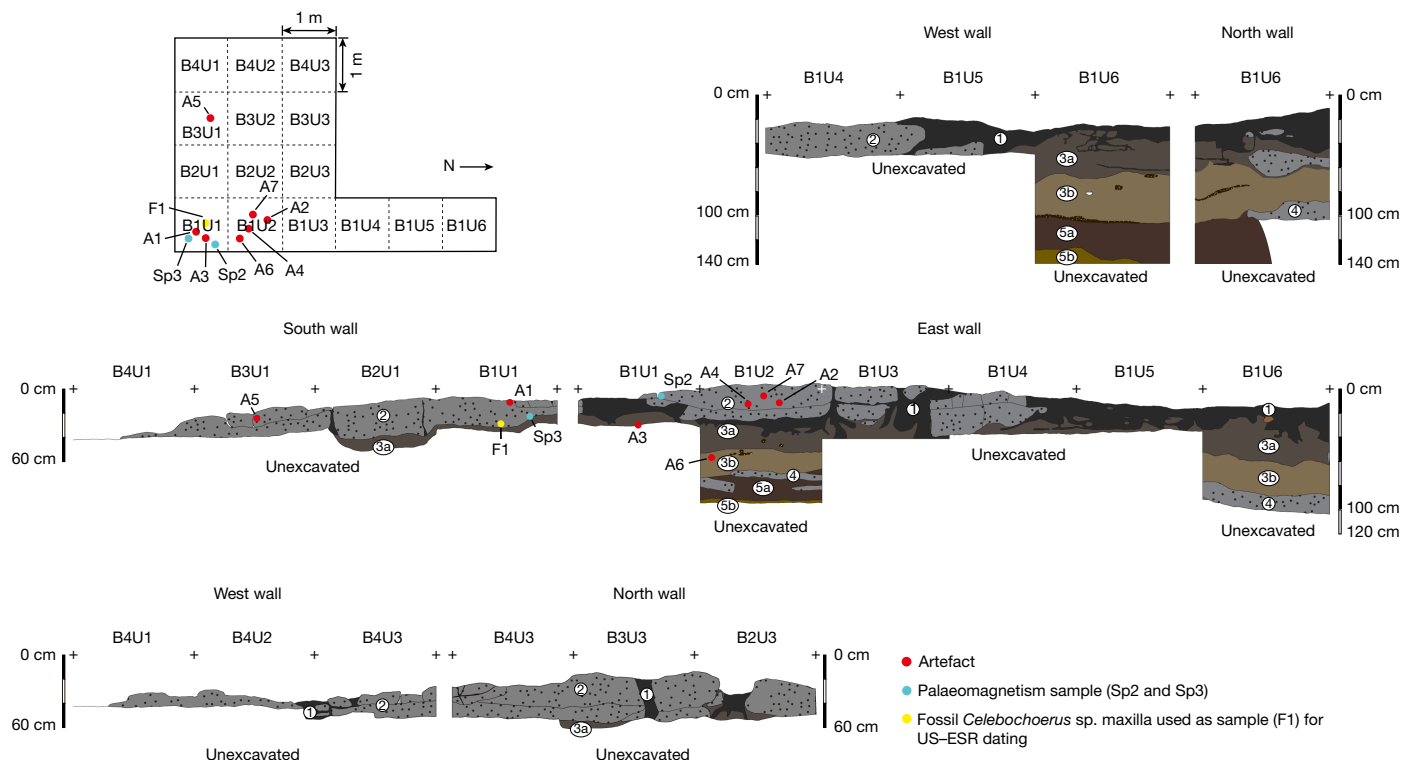


**Fig. 3 | Plan and stratigraphic sections of the Calio excavation.** Layer 1 is a dark brown topsoil with a sandy clay texture (maximum thickness of >40 cm in B1U3). Layer 2 is a grey conglomerate rock composed of tightly cemented sand and gravel containing various rock types, along with stone artefacts and extinct fossil fauna. This conglomerate layer covers almost the entire surface of the excavation units, except for squares B1U5 and B1U6. Layers 3a and 3b share similarities in both colour and texture, consisting of brown, dark brown and yellowish-brown sandy gravel layers with tabular cross-bedding, but moderately cemented. Layer 4 is similar to layer 2, a conglomerate sediment, but it is only found in a few excavation units, particularly squares B1U6 and B1U2. This layer

has a thickness of only about 5–10 cm and appears discontinuous, reappearing in other units, giving it an intercalated appearance. Layer 5a is dark brown with a sandy gravel texture. At the base of this layer, layer 5b consists of yellowish-brown sandy intercalations, contrasting in colour with the overlying layer but sharing the same sandy gravel texture. Layer 5c has a thickness of only 2–12 cm. At the base of layer 5b there is a layer resembling the conglomerate with similar characteristics, but it was not further excavated due to its extreme hardness. The deepest stone artefact (artefact 6; A6) was excavated from layer 3b at a depth of 56 cm in square B1U2. F1, the *Celebochoerus* maxilla dated using US–ESR.

approximately 56 cm below the surface in square B1U2 (Extended Data Figs. 2e and 3a–c). The artefacts are all lightly to heavily abraded and have sustained mechanical edge-flaking from fluvial transport, with these taphonomic scars showing contrasting amounts of abrasion on three artefacts. All stone artefacts are made of chert, alternately known as silicified limestone in some of the related literature<sup>14</sup>. This source material is abundantly present among the naturally occurring pebbles, but the stone artefacts differ statistically by their larger size compared with unmodified pebble-sized clasts ( $n = 179$ ; chert/silicified limestone, 83.2%; jasper, 8.9%; quartz, 5.6%; volcanics, 2.2%) excavated from the same fluvial sandstone deposits (Supplementary Information). An unpaired  $t$ -test indicates that the maximum dimension of the artefacts, an attribute measured independently from the technological length (which is measured along the percussion axis), is significantly longer than that of the natural pebbles (mean  $\pm$  s.d.:  $41.3 \pm 16.0$  mm versus  $18.5 \pm 9.1$  mm;  $t_{184} = 6.34$ ,  $P < 0.0001$ ). Similarly, there is a significant difference between the mean second longest measured dimension for both groups, with the artefacts ( $28.3 \pm 11.9$  mm) again being larger on average than the pebbles ( $11.9 \pm 6.5$  mm;  $t_{184} = 6.48$ ,  $P < 0.0001$ ) (Supplementary Fig. 8). These results suggest that the stone artefacts were produced by hominins outside the Calio site and carried there for use as tools, further underlining the anthropogenic origin of these objects. It is also possible that some or all artefacts could have been eroded out of riverbanks by laterally migrating fluvial channels, and may therefore be older than the layers in which they were found.

The flakes were struck by the hard-hammer freehand percussion technique and range from 21.9 to 60.1 mm long along the percussion

axes. Cortical surfaces were present on four flakes, and the nature of the cortex suggests that the stones targeted for flaking derived from local riverbeds. The orientation of dorsal flakes scars shows predominately unidirectional or, in one case (artefact 5), cross-axis reduction. Flakes were struck from relatively steep platforms ( $66.0 \pm 6.8^\circ$ ,  $n = 6$ ) by blows delivered from 2.6 to 19.7 mm from the core edge. Six flakes were struck from single-facet platforms, indicating rotation of the core during reduction. In one case (artefact 6), the core was rotated and the flake was struck from an adjoining face, removing a former platform surface. The previous flakes were struck at a steep angle from a cortical platform. The platform attributes on another flake (artefact 5) indicate that it was struck from a bifacial core edge. One artefact (artefact 2), a Kombewa flake<sup>23</sup>, was removed from the ventral surface of a larger flake and apparently then retouched unifacially to the dorsal surface along one edge. On another artefact (artefact 3), the radius of curvature on the single-facet platform suggests that it was also struck from a larger flake. The reduction of large flakes into smaller flakes, which were themselves retouched, suggests that a two-step reduction process was sometimes used to reduce the natural chert cobbles into suitably-sized tools. The evidence for reduction of cores-on-flakes, frequent core rotation and understanding of hard-hammer fracture mechanics attests to expert technical knowledge within the context of a straightforward, ‘least effort’ approach to toolmaking<sup>24</sup>.

We used palaeomagnetic dating and US–ESR dating to constrain the age of the artefact-bearing sediments at Calio. Concerning the former, a 12-m-thick sequence of coarse clastics alternating with sandy siltstones, which we interpret as a braided river sequence, was reconstructed by

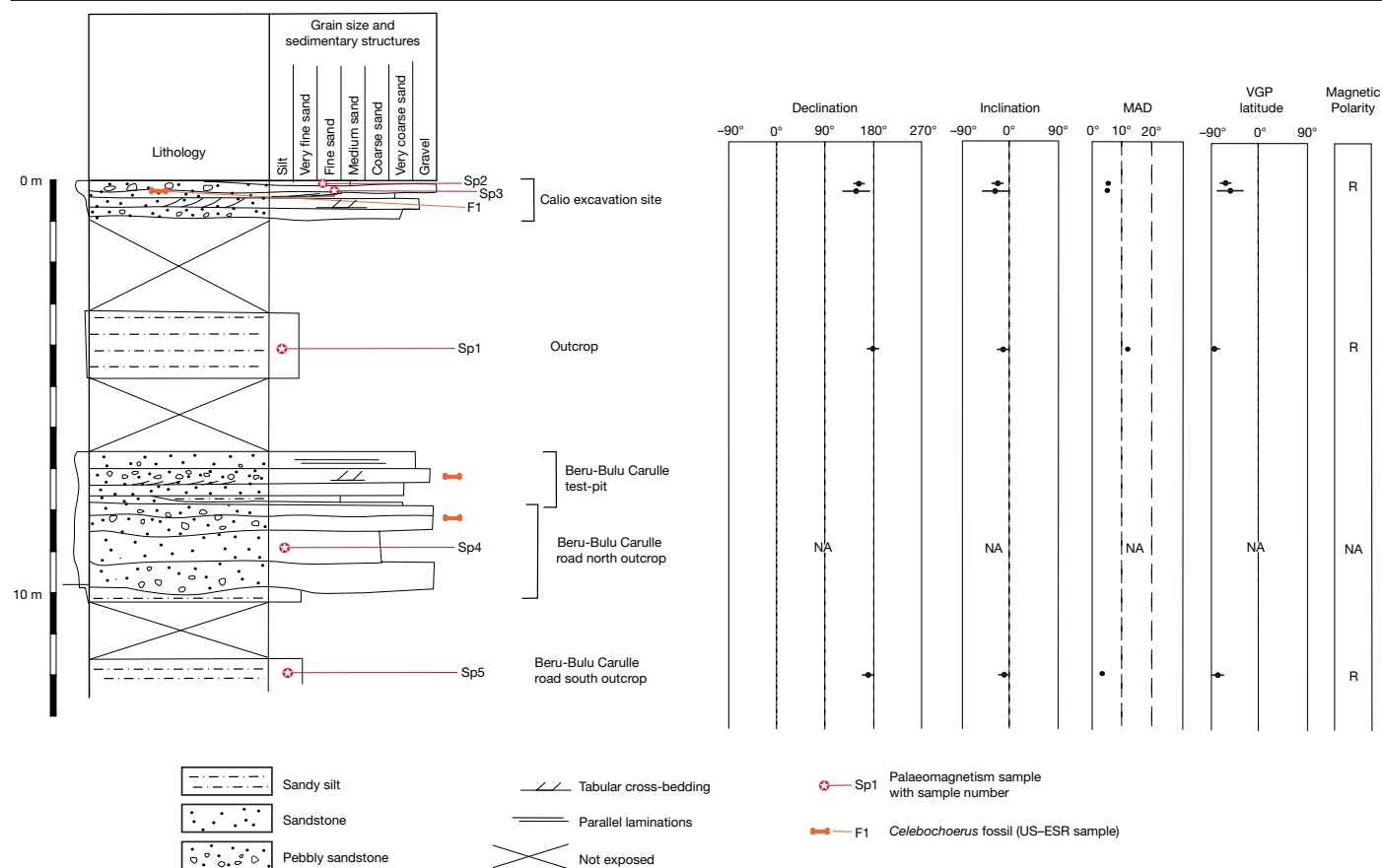


**Fig. 4 | The stratigraphic and palaeomagnetic context of the Calio site.**

Paleomagnetic results plotted along the stratigraphy of the Calio excavation site and Beru-Bulu Carulle test-pit 335 m to the east, as well as adjacent outcrops along the main road in the vicinity of Beru-Bulu Carulle (Extended Data Fig. 1d). The zero-elevation reference level is the datum used at the Calio excavation

site. Four samples taken within a stratigraphic interval of 12 m all returned reverse (R) magnetic polarities. One sample (Sp4) was broken in transit and could not be analysed further. MAD, mean angular deviation; NA, not available. The horizontal error bars indicate the 95% confidence limit of the mean directions ( $\alpha_{95}$ ) (Extended Data Table 2).

combining other outcrops in the vicinity of the Calio excavation site, including a 1-m-deep test-pit 335 m to the east of the latter at Beru-Bulu Carulle (Fig. 4 and Extended Data Figs. 1d and 5). Five oriented block samples (Sp1–Sp5) were taken at four finer-grained levels within this subhorizontal sequence, representing Beru Member Sub-Unit B (Extended Data Fig. 1d). An additional three samples were obtained from the Beru Member Sub-Unit A as exposed in the west-dipping west flank of the Sengkang Anticline, as well as six samples from the upper part of the underlying marine Samaoling Member (Extended Data Figs. 1d and 5). One sample (Sp4) was damaged during transport and could not be analysed further. The four samples collected in the immediate vicinity of the Calio excavation site all returned reliable reverse magnetic polarities (Fig. 4 and Extended Data Tables 1 and 2). Results indicate that the Beru Member Sub-Unit B sequence exposed near Calio (Fig. 4) should have a minimum age older than the boundary between the Brunhes Chron and Matuyama Chron at 773 ka (ref. 25). Some 130 m lower in the stratigraphic sequence, four samples taken at the base of the Beru Member Sub-Unit A also provided three reverse and one intermediate magnetic polarities (Extended Data Fig. 5 and Extended Data Tables 1 and 2). However, the large gap in data between the sampled intervals prohibits further correlations with the geomagnetic polarity time scale.

A palaeomagnetism age of older than 773 ka for the artefact-bearing layers at Calio is confirmed by US–ESR dating of two fossil teeth (left P<sup>4</sup> and left M<sup>3</sup>) from the *Celebochoerus* maxilla (Extended Data Fig. 4) excavated from the base of layer 2 (Extended Data Tables 3 and 4 and Supplementary Information). The assumption of immediate and

unchanged diffusion of uranium into the teeth at burial (EU model) has been criticized in the literature for its inaccuracy<sup>26</sup>. Thus, no scientifically relevant minimum age can be calculated. Alternatively, a maximum age of 2.1 Ma can be estimated, assuming that the uranium diffusion took place rapidly and at the time of the apparent U-series age. By doing so, we approximate a maximum age for the fossil and refer to the diffusion pattern as a closed-system U-series (CSUS). A more nuanced approach involves analysing uranium diffusion to ensure a comprehensive integration of uptake into the age calculation. Using the US–ESR approach, whereby uranium uptake is modelled using a diffusion coefficient ( $p$ ; Extended Data Fig. 6), we infer a likely age for the *Celebochoerus* maxilla of  $1.26 \pm 0.22$  Ma (Extended Data Tables 3 and 4), with individual ages of  $1.20 \pm 0.18$  Ma for the M<sup>3</sup> and  $1.43 \pm 0.21$  Ma for the P<sup>4</sup> (1 $\sigma$ ). The high uranium content in the M<sup>3</sup> dentine could potentially impact the ESR dose recovery, resulting in a younger age compared with the true depositional age (Extended Data Fig. 6). The negative impact of large amounts of uranium in dental tissues has been observed in other Indonesian fossils<sup>27</sup>. This phenomenon could be a result of high alpha emissions, although the exact cause is unknown<sup>28,29</sup>. In any case, it is generally only detrimental for ESR dating when uranium is concentrated in the enamel. As the uranium content is low (<1 ppm) in this part of the *Celebochoerus* teeth, this is unlikely to be a problem at Calio<sup>29</sup>.

Overall, the US–ESR-modelled results provide the most accurate age for fossil deposition and align well with the palaeomagnetism results. The deposits that yielded the stone artefacts at Calio most likely correspond in age to the reverse polarity interval between the Olduvai and Jaramillo Subchrons, broadly bracketing these layers to



between 1.787 Ma and 1.070 Ma (ref. 25). Although a post-Jaramillo age (<990 ka)<sup>25</sup> cannot be ruled out entirely considering the associated age error, the US–ESR results from the fossil teeth suggest that, statistically, the probability of a younger age is exceedingly low. As noted, the *Celebochoerus* maxilla was found at the base of layer 2 and therefore stratigraphically above the stratum (layer 3b) that yielded the lowermost stone artefact (Extended Data Figs. 2e and 3b,c). Thus, the modelled US–ESR average age (Supplementary Table 2) of  $1.26 \pm 0.22$  Ma for the dated fossil provides a minimum age of 1.04 Ma, and potentially up to 1.48 Ma, for the earliest proxy evidence for hominins at this site.

In summary, our findings demonstrate that in situ stone artefacts are present in fluvial sandstone layers of the Beru Member Sub-Unit B at Calio, and are therefore far earlier in age than what was formerly the oldest reported archaeological indication of hominins on Sulawesi (stone artefacts dated to about 194 ka at Talepu<sup>14</sup>). With a minimum age of 1.04 Ma, it now seems possible that hominin occupation of this large Wallacean island preceded that of Luzon<sup>6</sup> to the north and is at least as old as, and potentially earlier than, the hominin presence on Flores<sup>5,30</sup> to the south. However, precisely when hominins first crossed to Sulawesi remains an open question, as does the taxonomic affinity of the colonizing population.

## Online content

Any methods, additional references, Nature Portfolio reporting summaries, source data, extended data, supplementary information, acknowledgements, peer review information; details of author contributions and competing interests; and statements of data and code availability are available at <https://doi.org/10.1038/s41586-025-09348-6>.

- Hanebuth, T. J. J., Voris, H. K., Yokoyama, Y., Saito, Y. & Okuno, J. Formation and fate of sedimentary depocentres on Southeast Asia's Sunda Shelf over the past sea-level cycle and biogeographic implications. *Earth-Sci. Rev.* **104**, 92–110 (2011).
- Morwood, M. & van Oosterzee, P. *The Discovery of the Hobbit: The Scientific Breakthrough That Changed the Face of Human History* (Random House, 2007).
- Dennell, R. W., Louys, J., O'Regan, H. J. & Wilkinson, D. M. The origins and persistence of *Homo floresiensis* on Flores: biogeographical and ecological perspectives. *Quat. Sci. Rev.* **96**, 98–107 (2014).
- Ruxton, G. D. & Wilkinson, D. M. Population trajectories for accidental versus planned colonisation of islands. *J. Hum. Evol.* **63**, 507–511 (2012).
- Brumm, A. et al. Hominins on Flores, Indonesia, by one million years ago. *Nature* **464**, 748–752 (2010).
- Ingicco, T. et al. Earliest known hominin activity in the Philippines by 709 thousand years ago. *Nature* **557**, 233–237 (2018).
- Morwood, M. et al. Archaeology and age of a new hominin from Flores in eastern Indonesia. *Nature* **431**, 1087–1091 (2004).
- Morwood, M. et al. Further evidence for small-bodied hominins from the Late Pleistocene of Flores, Indonesia. *Nature* **437**, 1012–1017 (2005).
- Brown, P. et al. A new small-bodied hominin from the Late Pleistocene of Flores, Indonesia. *Nature* **431**, 1055–1061 (2004).
- Sutikna, T. et al. Revised stratigraphy and chronology for *Homo floresiensis* at Liang Bua in Indonesia. *Nature* **532**, 366–369 (2016).

- van den Bergh, G. D. et al. *Homo floresiensis*-like fossils from the early Middle Pleistocene of Flores. *Nature* **534**, 245–248 (2016).
- Kaifu, Y. et al. Early evolution of extremely small body size in *Homo floresiensis*. *Nat. Commun.* **15**, 6381 (2024).
- Détroit, F. et al. A new species of *Homo* from the Late Pleistocene of the Philippines. *Nature* **568**, 181–186 (2019).
- van den Bergh, G. D. et al. Earliest hominin occupation of Sulawesi, Indonesia. *Nature* **529**, 208–211 (2016).
- Westaway, K. E. et al. An early modern human presence in Sumatra 73,000–63,000 years ago. *Nature* **548**, 332–325 (2017).
- Hall, R. & Wilson, M. E. J. Neogene sutures in eastern Indonesia. *J. Asian Earth Sci.* **18**, 781–808 (2000).
- Grainger, A. M. & Davies, K. G. Reef exploration in the East Sengkang Basin, Sulawesi, Indonesia. *Mar. Pet. Geol.* **2**, 142–155 (1985).
- Jaya, A. & Nishikawa, O. Paleostress reconstruction from calcite twin and fault-slip data using the multiple inverse method in the East Walanae fault zone: implications for the Neogene contraction in South Sulawesi, Indonesia. *J. Struct. Geol.* **55**, 34–49 (2013).
- van den Bergh, G. D. The late Neogene elephantoid-bearing faunas of Indonesia and their palaeozoogeographic implications: a study of the terrestrial faunal succession of Sulawesi, Flores and Java, including evidence for early hominid dispersal east of Wallace's Line. *Scr. Geol.* **117**, 1–419 (1999).
- Bartstra, G.-J., Keates, S. G., Basoeki & Kallupa, B. On the dispersion of *Homo sapiens* in eastern Indonesia: the palaeolithic of South Sulawesi. *Curr. Anthropol.* **32**, 317–321 (1991).
- van Heekeren, H. R. The Tjabege flake industry from South Celebes. *Asian Perspect.* **2**, 77–81 (1958).
- Keates, S. G. & Bartstra, G.-J. Island migration of early modern *Homo sapiens* in Southeast Asia: the artifacts from the Walanae Depression, Sulawesi, Indonesia. *Palaeohistoria* **33/34**, 19–30 (1994).
- Owen, W. E. The Kombewa culture, Kenya Colony. *Man* **38**, 203–205 (1938).
- Isaac, G. L. in *Stone-Age Prehistory: Studies in Memory of Charles McBurney* (eds Bailey, G. N. & Callow, P.) 221–241 (Cambridge Univ. Press, 1986).
- Channell, J. E. T., Singer, B. S. & Jicha, B. R. Timing of Quaternary geomagnetic reversals and excursions in volcanic and sedimentary archives. *Quat. Sci. Rev.* **228**, 106114 (2020).
- Grün, R. The relevance of parametric U-uptake models in ESR age calculations. *Radiat. Meas.* **44**, 472–476 (2009).
- Rizal, Y. et al. Last appearance of *Homo erectus* at Ngandong, Java, 117,000–108,000 years ago. *Nature* **577**, 381–385 (2020).
- Duval, M. Evaluating the accuracy of ESR dose determination of pseudo-Early Pleistocene fossil tooth enamel samples using dose recovery tests. *Radiat. Meas.* **79**, 24–32 (2015).
- Duval, M. & Grün, R. Are published ESR dose assessments on fossil tooth enamel reliable? *Quat. Geochronol.* **31**, 19–27 (2016).
- van den Bergh, G. D. et al. An integrative tephro- and chronostratigraphic framework for the Pleistocene So'a Basin, central Flores (Indonesia) and its implications for faunal turnover and hominin arrival. *Quat. Sci. Rev.* **294**, 107721 (2022).

**Publisher's note** Springer Nature remains neutral with regard to jurisdictional claims in published maps and institutional affiliations.



**Open Access** This article is licensed under a Creative Commons Attribution-NonCommercial-NoDerivatives 4.0 International License, which permits any non-commercial use, sharing, distribution and reproduction in any medium or format, as long as you give appropriate credit to the original author(s) and the source, provide a link to the Creative Commons licence, and indicate if you modified the licensed material. You do not have permission under this licence to share adapted material derived from this article or parts of it. The images or other third party material in this article are included in the article's Creative Commons licence, unless indicated otherwise in a credit line to the material. If material is not included in the article's Creative Commons licence and your intended use is not permitted by statutory regulation or exceeds the permitted use, you will need to obtain permission directly from the copyright holder. To view a copy of this licence, visit <http://creativecommons.org/licenses/by-nc-nd/4.0/>.

© The Author(s) 2025

## Methods

### Palaeomagnetic analysis

Oriented block samples of approximately  $10 \times 10 \times 10 \text{ cm}^3$  each were carved with a sharp non-magnetic knife from fresh excavation baulks (samples Sp1 and Sp2) or from field exposures for palaeomagnetic analysis (Sp3–Sp14). Strike and dip were measured using a Brunton Compass corrected for local declination. Owing to the scarcity of suitable consolidated fine-grained layers, some samples were obtained from outcrops located up to 430 m from the measured section along the main Cabenge–Pampanua road (Extended Data Fig. 1). This stratigraphic section was originally recorded in 1991, when the outcrops along the road were still freshly exposed by construction works<sup>19</sup>. Five samples (Sp1–Sp5) were taken west of the Bulu Cepo Fault in subhorizontal to slightly west-dipping bedding, including two samples from the Calio excavation (Sp2 and Sp3), one sample from an outcrop along an erosional gully 74 m northwest of the Calio excavation (Sp1), one sample from the Beru (modern Indonesian spelling Berru) test-pit at 328 m eastsoutheast of the Calio Excavation (Sp4) and the fifth sample (Sp5) from an outcrop on the opposite side of the road 17 m south of the Beru test-pit. Samples Sp6 to Sp14 were obtained from steeply west-dipping layers east of the Bulu Cepo Fault. For those block samples taken at a distance from the road section, the approximate stratigraphic position relative to the section recorded in 1991 was extrapolated using the measured strike and dip of  $258^\circ/60^\circ$  (Extended Data Fig. 1d).

The carved samples were tightly packed in plastic and shipped to Bandung, Java, where they were further analysed at the Palaeomagnetism Laboratory of the Centre for Geological Survey (CGS). One sample (Sp4) arrived in a deteriorated condition and could not be analysed further. Of the remaining block samples, three to four  $1 \times 1 \times 1 \text{ cm}^3$  subsamples (denoted specimens and labelled sequentially) were carved from each, or, in cases in which the samples were not well consolidated, plastic cubes of the same dimensions were pressed into the sediments. Subsamples were stored in magnetically shielded containers to minimize viscous remanent acquisition of any modern magnetic field components. Care was taken to keep samples moist until palaeomagnetic measurements were made at the CGS Palaeomagnetic Laboratory.

Of all the palaeomagnetic block samples collected, three sequentially numbered subsamples (specimens) were then step-wise demagnetized with a Schonsted USA GSD-1 series alternating-field demagnetizer (AFD), at intervals of 2.5–5 mT, up to peak fields of 60–100 mT. If a fourth specimen was available, it was also step-wise demagnetized by thermal demagnetization (TD) using a magnetic measurement thermal demagnetizer MM80 series, at intervals of 100–25 °C, with a temperature up to 800 °C. Magnetic remanence directions and intensities were determined using a dual spinner magnetometer from AGICO (model JR-6A). Most of the samples were influenced by a secondary magnetization; however, this could be easily removed. Characteristic remanent magnetizations (ChRMs) were isolated throughout stepwise AFDs at 20–40 mT in level, above which most samples were completely demagnetized (Extended Data Fig. 7). Meanwhile, ChRMs were isolated through stepwise TDs at 200–300 °C to 550–600 °C, above which most samples were completely demagnetized (Extended Data Table 1 and Extended Data Fig. 8). The temperature range for ChRM indicates that magnetite is the dominant carrier of remanence. The ChRM directions obtained by TD are consistent with those obtained by AFD (Extended Data Table 1).

The ChRM is either trending to the origin of the orthogonal vector projections or is defined as the mean of vectors which are stable. Fisher's statistic was used to establish the mean direction of primary magnetism (Extended Data Table 2). The primary magnetic direction was determined from at least the last four to five plot points using principal component analysis<sup>31</sup>, with the mean maximum angular deviation set at  $<15^\circ$  using PuffinPlot software<sup>32</sup> and IAPD 2000 (ref. 33). Magnetic polarities are defined from the virtual geomagnetic pole (VGP) where

a normal polarity represents positive (Northern Hemisphere) VGP latitudes and a reverse polarity represents negative (Southern Hemisphere) VGP latitudes. Intermediate or transitional polarity fields are defined as those with VGP latitudes between  $45^\circ \text{ N}$  and  $45^\circ \text{ S}$ . Each VGP is calculated using the unit vector mean of the three to four directions observed at each sampling level.

Extended Data Fig. 9 shows the VGP plot of the 13 samples from the Calio excavation site and the samples taken further east. Twelve of the VGPs cluster in the Southern Hemisphere around the southern part of South Pacific Ocean and Antarctica, and all exhibit a reverse polarity. One sample (Sp9) has an intermediate or transitional VGP latitude of  $38.8^\circ \text{ S}$ , while another sample (Sp7) has a VGP latitude on the Northern Hemisphere (normal polarity).

The four samples associated with the subhorizontal fluvial beds of the Calio excavation site and Beru-Bulu Carulle test-pit west of the Bulu Cepo Fault all have a reverse polarity. This suggests that the sampled horizons have a minimum age of 773 ka, which corresponds to the Brunhes–Matuyama boundary<sup>25</sup>. On the basis of the US–ESR dating of the two *Celebochoerus* teeth, the approximately 12-m-thick sequence sampled at the excavation site and surrounding locales is more likely to pertain to the reverse magnetic interval below the Jaramillo Subchron (1,070–990 ka)<sup>25</sup>.

Three samples taken from the steeply west-dipping flank exposed at Ciangkange (Sp6, Sp10–11) also have a reverse polarity, while one sample (Sp9) shows an intermediate polarity (Extended Data Fig. 5). This interval is probably still within the Matuyama Chron. The normal polarity of sample Sp7 further down the sequence could be correlated to the Olduvai Subchron dated to 1.948–1.787 Ma (ref. 25), but this would need to be confirmed by a higher sampling density in the stratigraphy.

### U-series dating

U-series data were obtained by first sectioning a part of each of the two *Celebochoerus* fossil teeth using a high-precision diamond blade (300  $\mu\text{m}$  width) to expose both dental tissues. The exposed surface of each sample was then polished to  $>10 \mu\text{m}$  smoothness to provide a clean ablation surface. U-series measurements were undertaken by laser-ablation multi-collector-inductively coupled plasma mass spectrometry (MC-ICPMS) at the Geoarchaeology and Archaeometry Research Group (GARG) Biomics facility at Southern Cross University. Laser ablation was performed using a New Wave Research 193 nm Arf excimer laser, equipped with a TV2 cell. Thorium ( $^{230}\text{Th}$ ,  $^{232}\text{Th}$ ) and uranium ( $^{234}\text{U}$ ,  $^{235}\text{U}$ ,  $^{238}\text{U}$ ) isotopes were measured on the Thermo Neptune XT MC-ICPMS system mounted with jet sample and x-skimmer cones. All five isotopes were collected in static mode, with both  $^{234}\text{U}$  and  $^{230}\text{Th}$  collected in the ion counter and CDD respectively. Helium flow rate (850  $\text{ml min}^{-1}$ ), nitrogen (6  $\text{ml min}^{-1}$ ) and ICP-MS parameters were tuned with NIST610 element standard to derive a  $^{232}\text{Th}/^{238}\text{U}$  ratio of greater than 0.85 and therefore minimizing differences in fractionation between Th and U. Tuning was achieved with a fluence of about  $6.5 \text{ J cm}^{-2}$ , pulse rate of 100 Hz, spot size of 120  $\mu\text{m}$  and scan speed of  $5 \mu\text{m s}^{-1}$ , yielding 4.40 V of  $^{238}\text{U}$  and 3.85 V of  $^{232}\text{Th}$  on NIST610.

The *Celebochoerus* maxillary teeth were ablated using rasters of ~5 min each (twice ~800  $\mu\text{m}$  long). Before and after each sample, NIST612, MK10 and MK16 standards were measured<sup>34</sup>, as well as a fossil rhinoceros tooth with known isotopic ratios<sup>35</sup>. The  $^{234}\text{U}/^{238}\text{U}$  and  $^{230}\text{Th}/^{238}\text{U}$  isotopic ratios were corrected for elemental fractionation and Faraday cup/SEM yield by comparison with MK10 coral for which ratios were previously characterized internally by solution analysis<sup>34</sup>. Detrital-corrected  $^{230}\text{Th}$ -U ages were calculated for each analysis using IsoPlotR<sup>36</sup> and UThwig<sup>37</sup> with an assumed detrital ( $^{230}\text{Th}/^{232}\text{Th}$ ) activity ratio of  $0.8 \pm 0.8$  (ref. 38). Concentrations of U and Th were determined using NIST612 glass as a calibration standard. Background subtraction, concentration quantification and ratio corrections were performed using Iolite software<sup>39</sup>. The corrected  $^{234}\text{U}/^{238}\text{U}$  and  $^{230}\text{Th}/^{238}\text{U}$  isotope ratios for the secondary standard (MK16 coral) within error of the value

were determined by solution analysis. The rhinoceros tooth was used as a control for matrix effect.

Little to no detrital thorium was measured within the dental tissues, except at the surface and along cracks containing sediment intrusion (Extended Data Table 3). For the measurements, we avoided macroscopically visible cracks and obvious altered zones. The distribution of uranium across the dentine and the enamel is characteristic of the uranium diffusion pattern described in ref. 40. Uranium diffused from the pulp cavity across the dentine and accumulated at the enamel–dentine junction before diffusing slowly into the enamel crystal structure. This translates into a large variability of uranium content at the interface of the two tissues (Extended Data Table 3). In summary, the *Celebochoerus* teeth from Calio exhibit varying uranium distribution patterns (Extended Data Table 3), including heterogeneous age distributions, as well as uranium accumulation in altered zones and along the enamel–dentine junction. Such values across dental tissues are characteristic of the complex diffusion history of ancient fossil teeth with several diffusion episodes, localized uranium hotspots and leaching zones, especially close to the pulp cavity and along cracks, as well as other alterations in the dental tissues<sup>40</sup>.

### US–ESR dating

The ESR dating was carried out on the *Celebochoerus* fossil teeth (left P<sup>4</sup> and left M<sup>3</sup>). The outer layer of enamel was extracted mechanically from dentine with a rotary saw and cleaned carefully of any dentine residue (outer  $\sim 100\ \mu\text{m} \pm 10\%$  on each side). The P<sup>4</sup> tooth enamel was then ground into powder and sieved to 90–180  $\mu\text{m}$  before being split into 10 aliquots (about 95–100 mg each). While one aliquot was kept as a natural dose, the other nine aliquots received gamma irradiation steps of 50, 100, 250, 600, 1,200, 2,400, 4,000, 8,000 and 15,000 Gy at the Australian Nuclear Science and Technology Organisation. The aliquots were irradiated by a calibrated Gammacell 220 (<sup>60</sup>Co) gamma source with a dose rate of  $\sim 23.8\ \text{Gy min}^{-1}$ . The M<sup>3</sup> enamel was kept as a fragment, and this fragment was mounted into a parafilm mould within a Teflon sample holder to record the angular dependency in the ESR response<sup>41–44</sup>. Irradiation of the fragment was performed with the Freiberg X-ray irradiation chamber for fragments, which contains a Varian VF50 X-ray gun at a voltage of 40 kV and 0.5 mA current on the fragment exposed to X-rays without shielding (apart from a 200  $\mu\text{m}$  aluminium foil layer)<sup>45,46</sup>. Each fragment was irradiated after exponentially increasing irradiation times (at 90 s, 380 s, 900 s, 1,800 s, 3,600 s, 7,200 s, 14,400 s). For each irradiation step, the energy output of the X-ray gun was recorded at the beginning and end and then averaged, enabling us to correct for the dose rate received. For each irradiation step, the fragment was measured over 180° in x, y and z configurations with a 30° step<sup>41,43</sup>.

ESR intensities of tooth enamel powder were calculated using calibrated quartz tubes and measured using a Freiberg MS5000 ESR spectrometer at the GARG facility. Each tube was rotated three times with a 120° increment. All measurements (powder and fragment) were performed with the following conditions: 2 mW microwave power, 100 kHz modulation frequency with 1,024 points resolution, 0.1 mT modulation amplitude, 45 s conversion time, 12 mT sweep width and 21 s sweep time. The ESR intensities and dose–response curves followed previously reported recommendations<sup>29</sup>. The  $D_E$  was determined using the McDoseE 2.0 program<sup>47</sup>. Both single saturated exponential (SSE) function and double saturated exponential (DSE) function were applied to obtain  $D_E$  values, and both functions provided statistically undistinguishable results (P<sup>4</sup>: DSE,  $2,275 \pm 124\ \text{Gy}$ ; and SSE,  $2,267 \pm 99$ ; M<sup>3</sup>: DSE,  $2,140 \pm 108\ \text{Gy}$ ; and SSE,  $2,116 \pm 118$ ). Yet, it is our experience that SSE provides more systematic and reliable results than DSE, as long as recommendations from ref. 29 are followed.

ESR intensities were extracted from T1–B2 peak-to-peak amplitudes on the merged ESR signal or the powder spectra<sup>41</sup>. Isotropic and baseline corrections were applied uniformly across the measured spectra for

fragment measurements<sup>42</sup>. The amount of unstable non-orientated CO<sub>2</sub> radicals (NOCORs) was estimated on the fragment irradiated by X-ray to be negligible ( $\sim 1\%$ ) and, therefore, could not be applied to the powder sample (M<sup>3</sup>) using the protocol described previously<sup>41</sup>. The results of the gamma rays irradiated powder are consequently uncorrected for NOCORs. The ESR dose–response curves for the fragment were obtained using merged ESR intensities of all orientations and associated s.d. values from the repeated measurements over one orientation only. For powder spectra, associated s.d. values were obtained using repeated measurements after shaking the tube at each irradiation step.

Sediment elemental concentrations, external beta and gamma dose rate contributions, and water content (measured) are shown in Extended Data Table 4. The external beta dose rates have been extrapolated from the U, Th and K contents measured on the associated sediment ( $\sim 50\ \text{g}$ ). The sediments were collected in the immediate vicinity of the sample. The sediment was crushed, homogenized and separated into three aliquots before being digested in a 1:3 nitric/HCl acid solution (APHA 3125 ICPMS). The external gamma dose rates were determined using the associated sediment and assuming a  $4\pi$  geometry. The cosmic dose rate was estimated based on consideration of the altitude, geomagnetic latitude and density ( $2\ \text{g cm}^{-3}$ ) of sediment overburden<sup>48</sup>. However, a large part of the ancient sedimentary deposit (probably several metres in thickness) at the Calio locality has clearly eroded away over time, leaving only a 30 cm depth for the current burial sample.

The internal dose rate was calculated from the U-series measurements obtained on each enamel fragment and surrounding dentine. Both enamel and dentine were measured using rasters (see the U-series dating description above for parameters). Concentration and isotopic ratios were measured directly on the fragment used, and all measurements were averaged to obtain a single value for the entire tooth. Post-Rn equilibrium was assumed. Ages were calculated using dose rate conversion factors described previously<sup>49</sup>. Moreover, ESR ages were calculated using both the US–ESR MATLAB program<sup>50</sup> and the DATA program<sup>51</sup> to compare US–ESR results, and with DATA to obtain closed-system calculation (CSUS–ESR age estimation).

### Stone artefact analysis

The stone artefacts excavated from Calio were analysed using qualitative and quantitative methods published elsewhere<sup>52–54</sup>. Artefact condition was assessed according to criteria outlined in Shea<sup>55</sup>, with taphonomic abrasion and edge-damaged considered separately. Artefact material is classified as chert in all cases pending closer assessment of local stone sources.

Technological length refers to the measurement from the point of force application (PFA) to the distal end of the flake along the percussion axis. Technological width is the maximum width at right angles to technological length. Thickness refers to maximum thickness at right angles to the plane defined by technological length and width. Maximum length and width are the maximum dimensions of the flake, along any axis. Thickness was also measured at 25%, 50% and 75% of the distance from the PFA to the distal end, as a proxy for morphological uniformity.

Platforms describe the nature of the surface marked by the PFA. Platform depth is the distance from the PFA to the dorsal platform edge, as measured along the plane defined by the percussion axis. Platform width measures the maximum width of the flake's platform<sup>56</sup>. The number of flake scars on the platform surface was counted.

Exterior platform angles were measured using a lockable sliding bevel gauge combined with a digital goniometer. One arm of the sliding bevel was placed along the dorsal flake surface and the second arm was placed along the platform surface, from the dorsal platform edge to the PFA. The bevel was locked and the angle between the gauge's arms was measured using the digital goniometer. The interior platform angle was measured directly using the digital goniometer. One arm was placed along the platform surface from the dorsal platform edge to the PFA,



# Article

and the other arm was placed along the surface within 1–2 mm below the PFA, along the side of the hertzian cone at the start of the bulb of percussion, as described previously<sup>57</sup>.

The sizes of retouching scars measuring >2 mm in maximum dimension were recorded. Length was measured from the existing platform edge to the distal edge, along the percussion axis. Width was measured at right angles to length. Cortex proportion was assessed visually as described previously<sup>58</sup>. Cortex on platforms was included in the assessment of cortex coverage. The location of cortex was recorded as described previously<sup>59</sup>.

Flake types were recorded as described previously<sup>60</sup>, where type IV refers to flakes with non-cortical platforms and 100% dorsal cortex coverage; type V refers to flakes with non-cortical platforms and partial dorsal cortex coverage; and type VI refers to flakes with non-cortical platforms and no dorsal cortex (types I–III were not present in the Calio assemblage). Dorsal scar orientations followed the sector approach described previously<sup>61</sup>, excluding the redirecting flake.

Annotated 3D photogrammetric models were made of the Calio artefacts according to protocols described previously<sup>62</sup>. The photographs were taken using a Nikon D7200 camera with AF-S DX Nikkor 18–140 mm lens and processed with Agisoft Metashape v.2.0.1.16069. The 3D models can be accessed online (<https://une.pedestal3d.com/r/ZdPcP-kXvc/>).

The Calio artefact data are presented in Supplementary Table 1. Incomplete linear dimensions are recorded as negative values and highlighted in red font.

## Reporting summary

Further information on research design is available in the Nature Portfolio Reporting Summary linked to this article.

## Data availability

The data supporting the findings of this study are provided in the Supplementary Information. Raw and additional source data are available from publicly available Zenodo<sup>65</sup> data repositories (available at <https://doi.org/10.5281/zenodo.15515771>). Access to primary archaeological assemblages (such as stone artefacts, fossil fauna) is available to researchers on reasonable request.

31. Kirschvink, J. L. The least-squares line and plane and the analysis of palaeomagnetic data. *Geophys. J. Int.* **62**, 699–718 (1980).
32. Lurcock, P. C. & Wilson, G. S. PuffinPlot: a versatile, user-friendly program for paleomagnetic analysis. *Geochem. Geophys. Geosyst.* **13**, Q06Z45 (2012).
33. Torsvik, T. H., Briden, J. C. & Smethurst, M. A. Super-IAPD: interactive analysis of palaeomagnetic data. *Geodynamics.no* [www.geodynamics.no/Web/Content/Software/](http://www.geodynamics.no/Web/Content/Software/) (2000).
34. Woodroffe, C. D., Short, S. A., Stoddart, D. R., Spencer, T. & Harmon, R. S. Stratigraphy and chronology of late Pleistocene reefs in the Southern Cook Islands, South Pacific. *Quat. Res.* **35**, 246–263 (1991).
35. Grün, R., Eggins, S., Kinsley, L., Moseley, H. & Sambridge, M. Laser ablation U-series analysis of fossil bones and teeth. *Palaeogeogr. Palaeoclimatol. Palaeoecol.* **416**, 150–167 (2014).
36. Vermeesch, P. IsoplotR: a free and open toolbox for geochronology. *Geosci. Front.* **9**, 1479–1493 (2018).
37. Dosseto, A. & Marwick, B. UThwigl—an R package for closed- and open-system uranium–thorium dating. *Quat. Geochronol.* **67**, 101235–101248 (2022).
38. Paul, D., White, W. M. & Turcotte, D. L. Constraints on the <sup>232</sup>Th/<sup>238</sup>U ratio (k) of the continental crust. *Geochem. Geophys. Geosyst.* **4**, 1102 (2003).
39. Paton, C. et al. Iolite: freeware for the visualisation and processing of mass spectrometric data. *J. Anal. At. Spectrom.* **26**, 25082518 (2011).
40. Grün, R., Aubert, M., Joannes-Boyau, R. & Moncel, M. H. High-resolution analysis of uranium and thorium concentration as well as U-series isotope distributions in a Neanderthal tooth from Payre using laser ablation ICP-MS. *Geoch. Cosm. Acta.* **72**, 5278–5290 (2008).
41. Joannes-Boyau, R. Detailed protocol for an accurate non-destructive direct dating of tooth enamel fragment using electron spin resonance. *Geochronometria* **40**, 322–333 (2013).

42. Joannes-Boyau, R. & Grün, R. Thermal behavior of oriented and non-oriented CO<sub>2</sub><sup>•−</sup> radicals in tooth enamel. *Radiat. Meas.* **44**, 505–511 (2009).
43. Joannes-Boyau, R. & Grün, R. A comprehensive model for CO<sub>2</sub><sup>•−</sup> radicals in fossil tooth enamel: implications for ESR dating. *Quat. Geochron.* **6**, 82–97 (2011).
44. Joannes-Boyau, R., Bodin, T. & Grün, R. Decomposition of the angular ESR spectra of fossil tooth enamel fragments. *Radiat. Meas.* **45**, 887–898 (2010).
45. Grün, R., Mahat, R. & Joannes-Boyau, R. Ionization efficiencies of alanine dosimeters and tooth enamel irradiated by gamma and X-ray sources. *Radiat. Meas.* **47**, 665–668 (2012).
46. Yu, W., Herries, A. I. & Joannes-Boyau, R. Using X-rays as an irradiation source for direct ESR dating of fossil teeth. *Quat. Geochronol.* **72**, 101372 (2022).
47. Joannes-Boyau, R., Duval, M. & Bodin, T. MCDoseE 2.0. A new Markov chain Monte Carlo program for ESR dose response curve fitting and dose evaluation. *Quat. Geochron.* **44**, 13–22 (2018).
48. Prescott, J. R. & Hutton, J. T. Cosmic ray contributions to dose rates for luminescence and ESR 583 dating: large depths and long-term time variations. *Radiat. Meas.* **23**, 497–500 (1994).
49. Guérin, G., Mercier, N. & Adamiec, G. Dose rate conversion factors: update. *Ancient TL* **29**, 5–8 (2011).
50. Shao, Q., Bahain, J. J., Dolo, J. M. & Falguères, C. Monte Carlo approach to calculate US-ESR age and age uncertainty for tooth enamel. *Quat. Geochron.* **22**, 99–106 (2014).
51. Grün, R. The DATA program for the calculation of ESR age estimates on tooth enamel. *Quat. Geochron.* **4**, 231–232 (2009).
52. Moore, M. W., Sutikna, T., Jatmiko, Morwood, M. J. & Brumm, A. Continuities in stone flaking technology at Liang Bua, Flores, Indonesia. *J. Hum. Evol.* **57**, 503–526 (2009).
53. Moore, M. W. et al. Archaeology and art in context: excavations at the Gulu Site Complex, Northwest Kimberley, Western Australia. *PLoS ONE* **15**, e0226628 (2020).
54. Moore, M. W. et al. Bronze age stone flaking at Saruq al-Hadid, Dubai, southeastern Arabia. *PLoS ONE* **17**, e0270513 (2022).
55. Shea, J. J. Artifact abrasion, fluvial processes, and “living floors” from the Early Paleolithic site of ‘Ubeidiya (Jordan Valley, Israel). *Geoarchaeology* **14**, 191–207 (1999).
56. Lin, S. C. et al. The mediating effect of platform width on the size and shape of stone flakes. *PLoS One* **17**, e0262920 (2022).
57. Li, L., Reeves, J. S., Lin, S. C., Tennie, C. & McPherron, S. P. Quantifying knapping actions: a method for measuring the angle of blow on flakes. *Archaeol. Anthropol. Sci.* **14**, 156 (2022).
58. Dibble, H. L., Schurmans, U. A., Iovita, R. P. & McLaughlin, M. V. The measurement and interpretation of cortex in lithic assemblages. *Am. Antiq.* **70**, 545–560 (2005).
59. Toth, N. & Schick, K. in *The Oldowan: Case Studies into the Earliest Stone Age* (eds Toth, N. & Schick, K.) 3–42, Publication Series no. 1. (Stone Age Institute Press, 2006).
60. Toth, N. The Oldowan reassessed: a close look at early stone artifacts. *J. Archaeol. Sci.* **12**, 101–120 (1985).
61. Tostevin, G. B. *Seeing Lithics: A Middle-Range Theory for Testing for Cultural Transmission in the Pleistocene* (Oxbow Books, 2012).
62. Mallison, H. & Wings, O. Photogrammetry in paleontology—a practical guide. *J. Paleontol. Tech.* **12**, 1–31 (2014).
63. Grün, R., Schwarcz, H. & Zymela, S. Electron spin resonance dating of tooth enamel. *Can. J. Earth Sci.* **24**, 1022–1037 (1986).
64. Grün, R. An alternative model for open system U-series/ESR age calculations: (closed system U-series)-ESR, CSUS-ESR. *Anc. TL* **18**, 1–4 (2000).
65. Hakim, B. et al. Data for ‘Hominins on Sulawesi during the Early Pleistocene’. *Zenodo* <https://doi.org/10.5281/zenodo.15515771> (2025).

**Acknowledgements** This research was funded by a research grant awarded to B.H. by Indonesia’s National Research and Innovation Agency (Badan Riset dan Inovasi Nasional (BRIN)) and an Australian Research Council (ARC) Future Fellowship awarded to A.B. (FT160100119), with further financial support from Griffith University. We thank the staff at BRIN and the Regent (Bupati) of the Soppeng government H. Andi Kaswadi Razak for permission to conduct the fieldwork investigations, and for other practical and logistical support. We acknowledge the assistance provided by Balai Pelestarian Kebudayaan (BPK) Region XIX and the Sulawesi Archaeological Research Center (Universitas Hasanuddin (UNHAS)-BRIN). Field assistance was provided by S. Yakub, A. A. Qalam, Siska, N. I. Amir and F. Reza from UNHAS, D. Susanti from BPK Region XIX and the following staff members from BRIN’s Makassar branch: Ernianti, Murniati, Muheminah, Lendrawati, D. Purnama, Y. Kurata, K. Saleh and H. Hamzah.

**Author contributions** B.H. conceived and led the research with specialist input from A.B.; U.P.W. and D.Y. conducted the palaeomagnetism study. G.D.v.d.B. performed key stratigraphic correlations in the field. Field assistance was provided by A.D., R.S., I.A.N., M.R.P., I.M., A.H., K.A.A., A.M.S., P.A.B., S.A., P.H.M., A.A., N.S., F., B.B. and Z.M.; M.W.M. conducted the lithic analysis with S. and Y.L.P.; US-ESR dating was undertaken by R.J.-B., W.Y. and M.A.; B.H., A.B. and G.D.v.d.B. wrote the manuscript, with editorial input from all of the authors.

**Competing interests** The authors declare no competing interests.

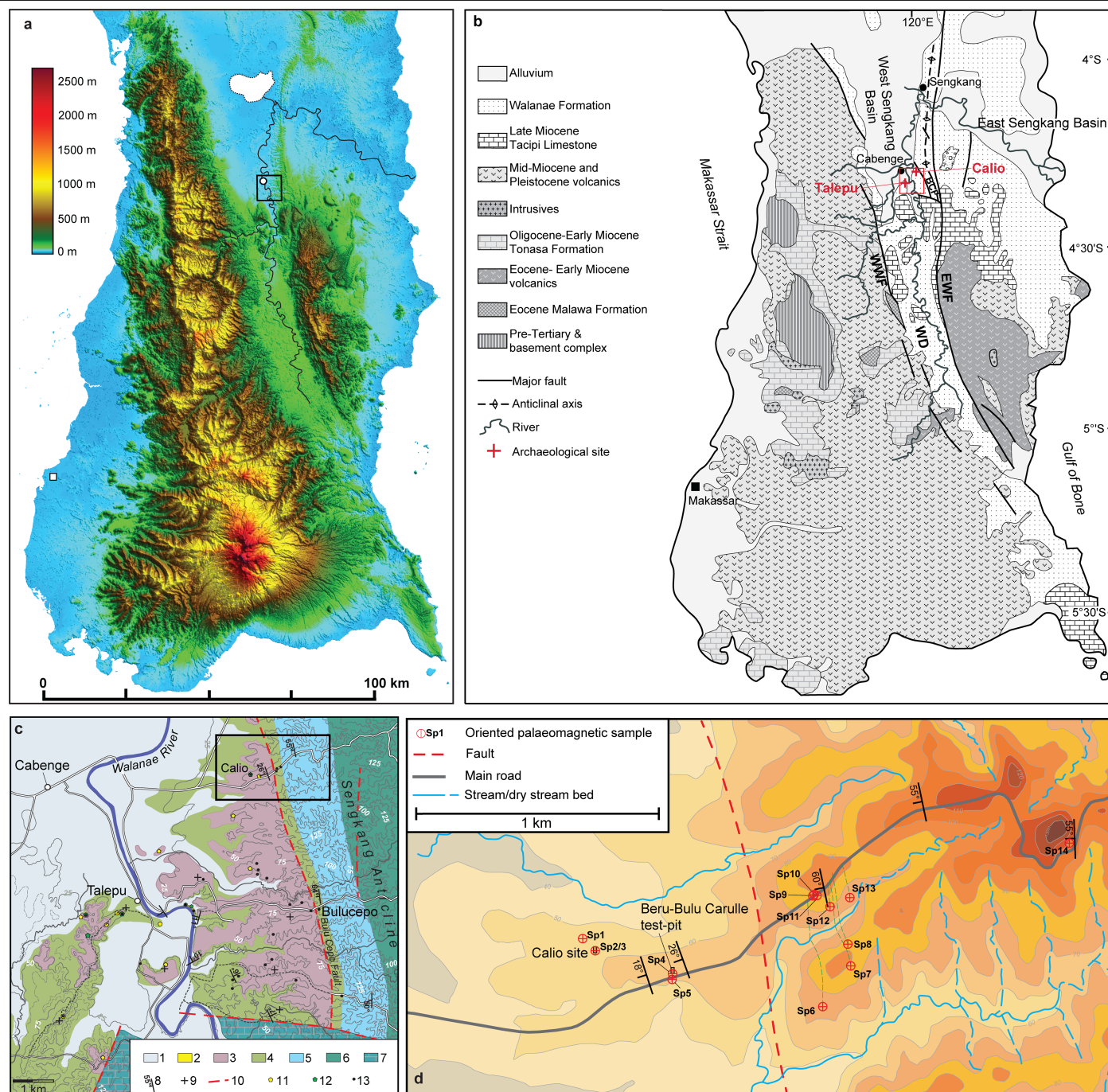
## Additional information

**Supplementary information** The online version contains supplementary material available at <https://doi.org/10.1038/s41586-025-09348-6>.

**Correspondence and requests for materials** should be addressed to Budianto Hakim or Adam Brumm.

**Peer review information** Nature thanks Florent Detroit, Mathieu Duval and Masayuki Hyodo for their contribution to the peer review of this work.

**Reprints and permissions information** is available at <http://www.nature.com/reprints>.



**Extended Data Fig. 1 | Geological and stratigraphic context of the Calio site.**

**a**, Digital Elevation Map of the southwestern peninsula of Sulawesi and **b**, Simplified geological map of the same area. Small red square indicates area shown in **c**, geological map of the study area. 1: Modern alluvium; 2: Late Pleistocene alluvial terrace; 3-7: Lithological sub-units of the Walanae Formation (3: Beru Member Sub-Unit B [fluvial facies]; 4: Beru Member Sub-Unit A [fluvio-estuarine facies]; 5: Samaoling Member [shallow marine facies]; 6: Burecing Member [deep marine facies]; 7: Tacipi Limestone Member); 8: strike and dip; 9:

horizontal bedding; 10: inferred fault; 11: sites with surface collected stone artefacts; 12: sites with in situ stone artefacts; 13: vertebrate fossil localities. Rectangle indicates the area surrounding Calio shown in **d**, contour map of the Calio excavation area showing the palaeomagnetic sampling sites (red circles). The stratigraphic section shown in Extended Data Fig. 5 was measured along the main road. Green dashed lines connect the sampling sites with the measured section, taking into account topography and strike and dip. Panels **a-c** modified after ref. 14.





Extended Data Fig. 2 | See next page for caption.



**Extended Data Fig. 2 | Calio archaeological site.** **a**, Location of the fossil- and stone artefact-bearing fluviatile pebbly sandstone strata outcropping at the ground surface in an agricultural field; **b-d**, Archaeological excavations at Calio (2022); **e**, 3D photogrammetry model of the excavated squares showing the locations of the stone artefacts and dated *Celebochoerus* fossil (F1) projected

onto the stratigraphy (scale bars, 10 mm). Layers 1 to 5b are labelled. The deepest stone artefact excavated at Calio (Artefact 6) was found 56 cm below the ground surface in layer 3b. Agisoft Metashape Professional was used to produce the 3D image and the finds were projected onto this model using ArcGIS Pro.



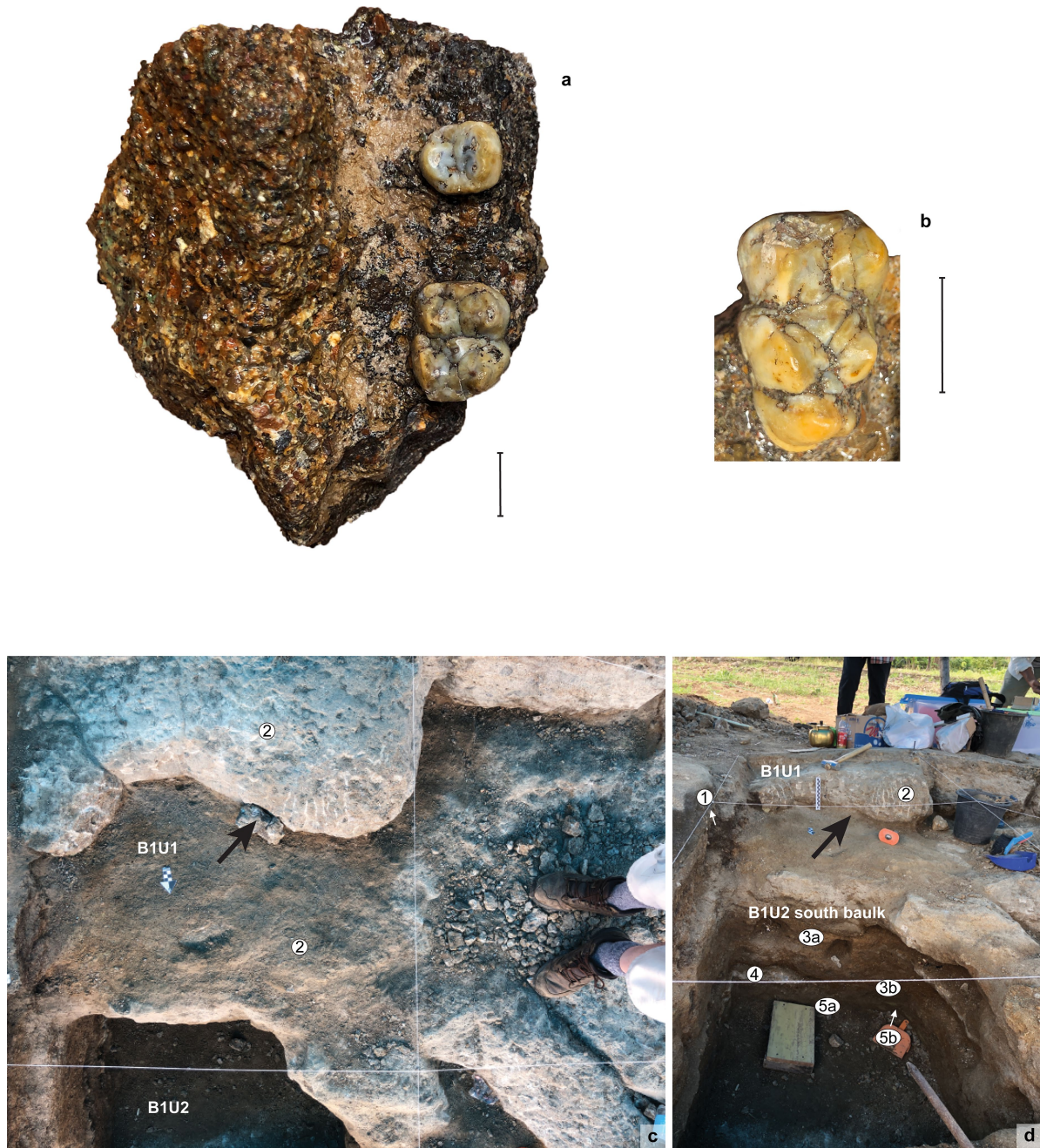
**Extended Data Fig. 3** | See next page for caption.

**Extended Data Fig. 3 | Stone artefacts in Early Pleistocene deposits at Calio.**

**a**, Overhead view of the Calio trench showing the locations of the stone artefacts and the dated fossil specimen (F1); **b**, 3D photogrammetry model of the trench (section A to B in panel **a**) with archaeological finds projected and sedimentary layers indicated (layers 1-5b) (Agisoft Metashape Professional was used to produce the 3D image and the finds were projected onto this model

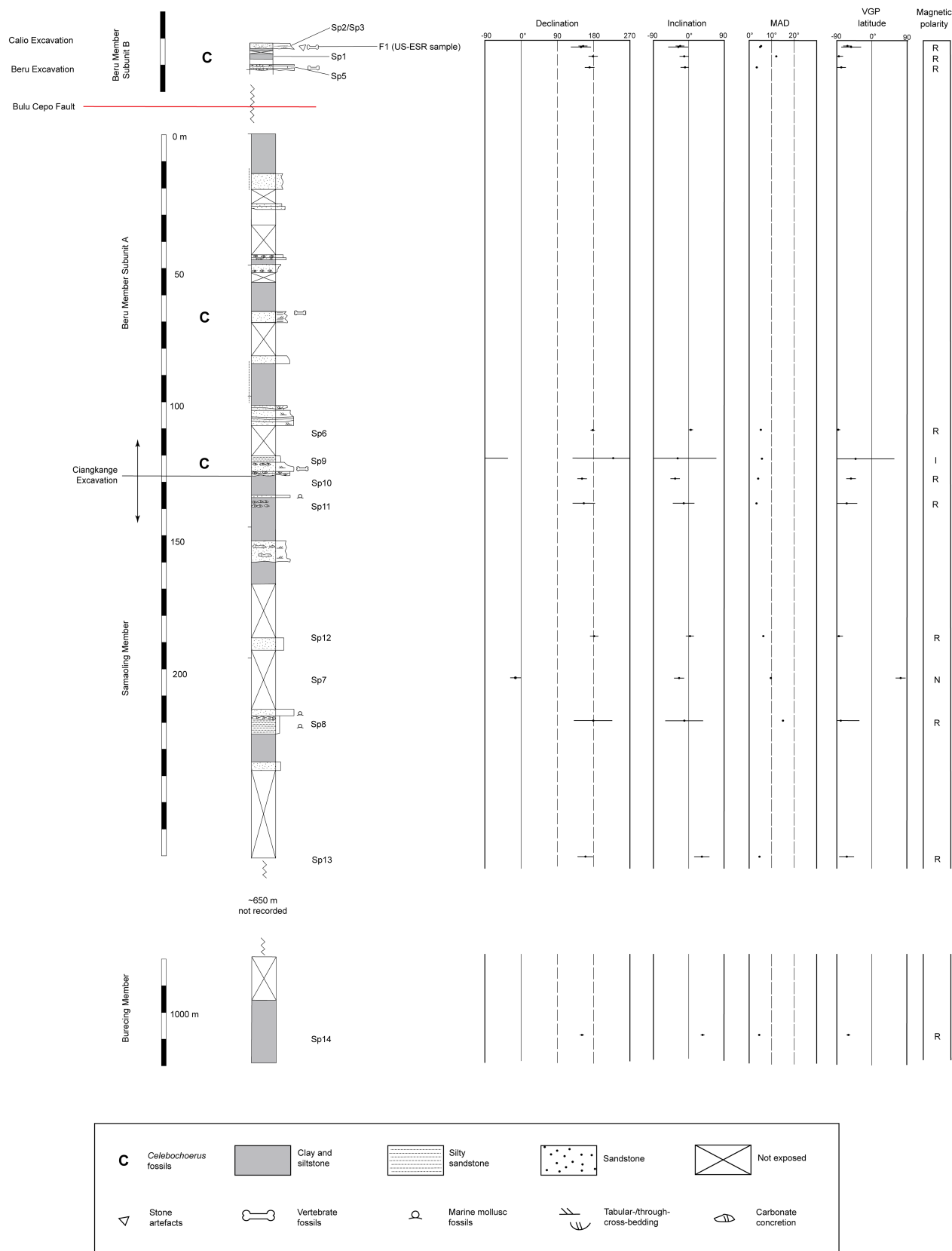
using ArcGIS Pro); **c**, The stratigraphically deepest stone artefact excavated from the site (Artefact 6), seen here exposed in layer 3b in the trench wall; **d**, Artefact 5; **e**, Artefact 2; **f**, Artefact 4; **g**, Artefact 1 exposed on the ground surface partially embedded in extremely hard fluvial sandstone comprising the capping conglomerate (layer 2).





**Extended Data Fig. 4 | *Celebochoerus heekereni* fossil maxilla fragment from Calio.** The specimen was embedded in coarse sandstone and retrieved in two separate fitting blocks found in the same location (black arrows in **c** and **d**). **a**, Occlusal view of sinistral P<sup>4</sup> and M<sup>2</sup>; **b**, Occlusal view of sinistral M<sup>3</sup> of the same individual retrieved from the opposite block; **c-d**, Find location of the dated

*Celebochoerus* fossil maxilla (marked by arrows) in square B1U1 approximately 30 cm below the ground surface. The deepest stone artefact (Artefact 6) was excavated from the adjoining square B1U2 to the north and was located -26 cm below the level of the fossil.

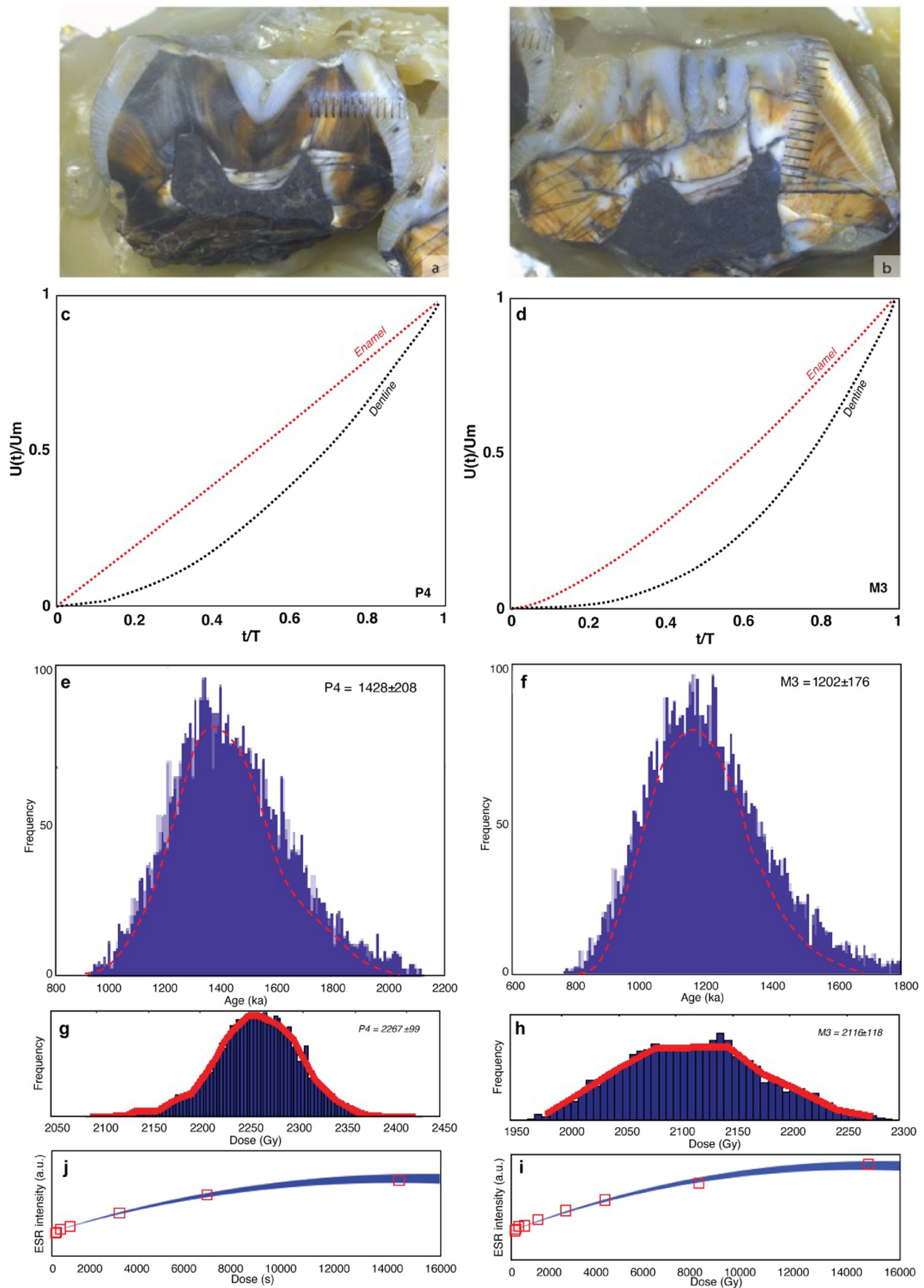


**Extended Data Fig. 5** | See next page for caption.

**Extended Data Fig. 5 | Stratigraphy and palaeomagnetic results of the upper part of the Walanae Formation, including the Calio excavation site.**

The stratigraphy is based on the Cabenge-Pampanua road section reported previously<sup>19</sup>. *Celebochoerus* icons indicate the fluvial deposits that contained vertebrate fossils as described in the prior study<sup>19</sup> and the current paper. The panel to the right shows the paleomagnetic results of 14 samples. The approximate stratigraphic levels of palaeomagnetic samples taken at a distance from the recorded road section are based on extrapolation using the measured strike and dip of 258°/60° (see Extended Data Fig. 1). Sample Sp9 yielded intermediate results. Horizontal error bars indicate the 95% confidence limit of the mean

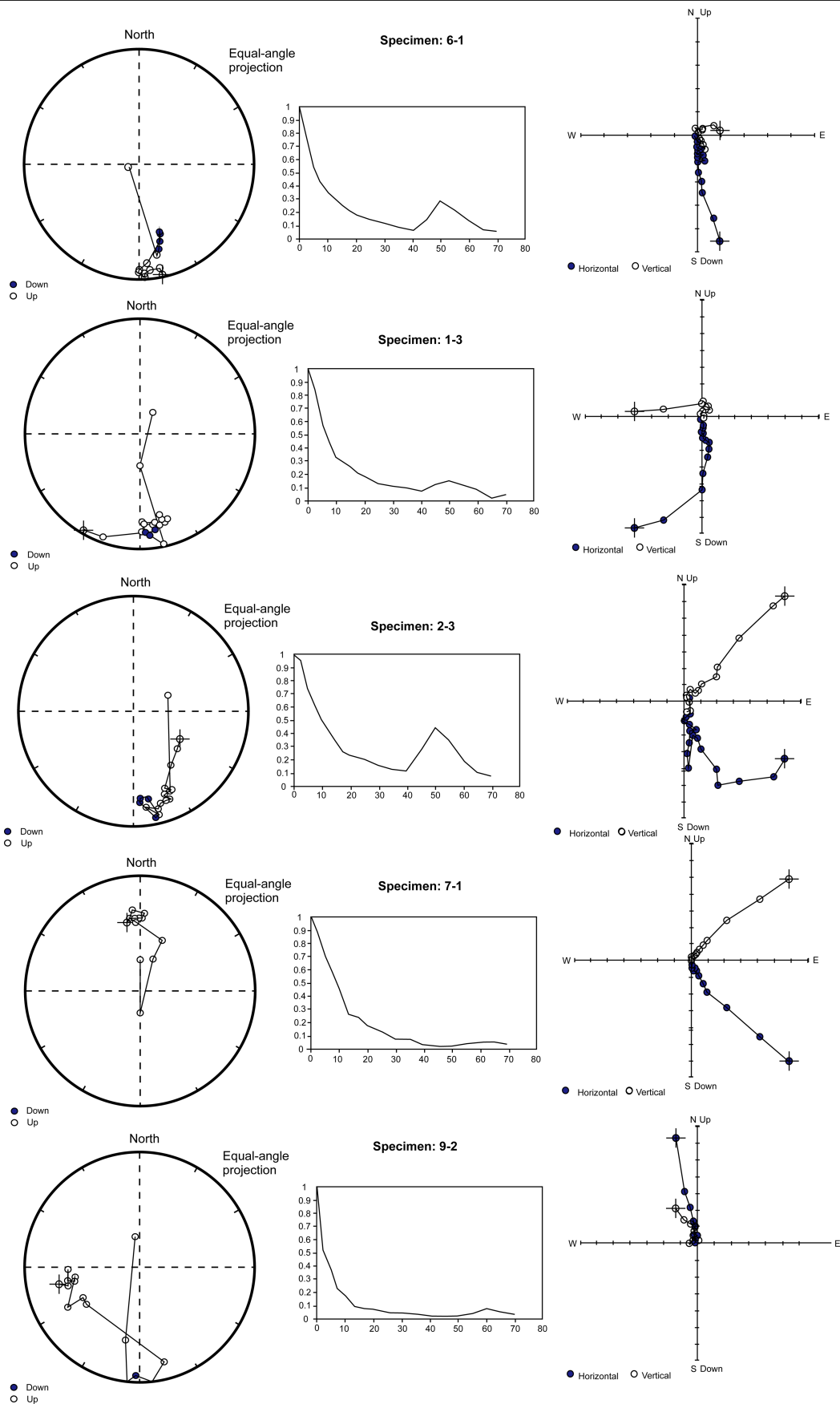
directions ( $\alpha_{95}$ ) (see Extended Data Table 2). The low sampling density does not allow for a correlation with the geomagnetic polarity time scale; however, the Reverse polarities near Ciangkange (Sp6 and Sp9 to Sp11) likely fall within the Matuyama Chron, because the top of the underlying marine Burecing Member (Sp14) contains nannofossils pertaining to nannoplankton zone CN12, which ranges in age from 3.75 to 1.95 Ma (ref. 19). R = Reverse polarity, N = Normal polarity, I = Intermediate polarity. F1 = *Celebochoerus* fossil maxilla excavated from the Calio site and dated using coupled Uranium-series and Electron Spin Resonance (US-ESR) to a minimum of 1.04 Ma.



**Extended Data Fig. 6 | US-ESR dating results for two *Celebochoerus* fossil teeth at Calio.** **a-b**, Cross-sections of the two teeth (**a**, premolar P<sup>4</sup>; **b**, molar M<sup>3</sup>). Uranium uptake model in dental tissues of **c**, P<sup>4</sup> and **d**, M<sup>3</sup>. Age distribution

likelihood for **e**, P<sup>4</sup> and **f**, M<sup>3</sup>. ESR dose equivalent (De) distribution likelihood of **g**, P<sup>4</sup> and **h**, M<sup>3</sup>. ESR dose response curve (DRC) calculation using the Monte Carlo algorithm of McDoseE 2.0; **i**, P<sup>4</sup> and **j**, M<sup>3</sup>.

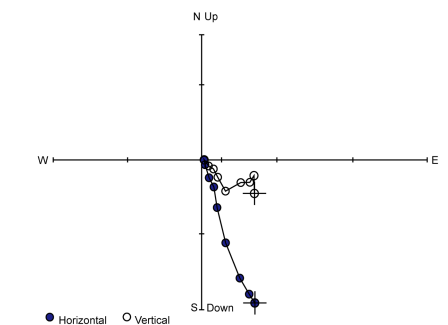
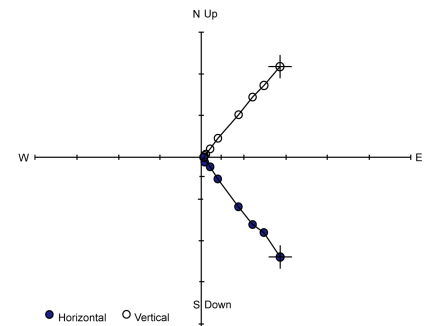
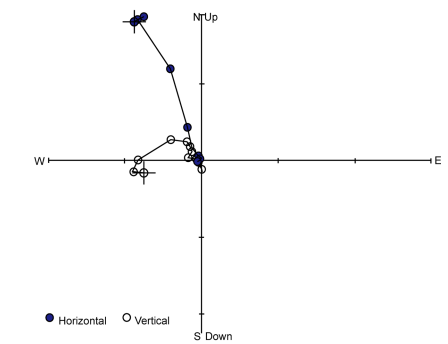
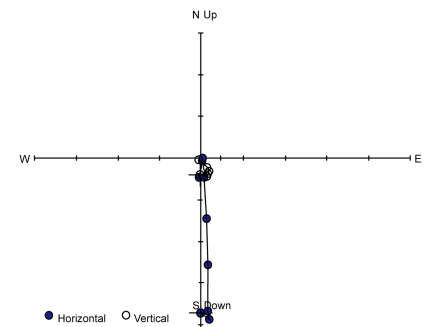
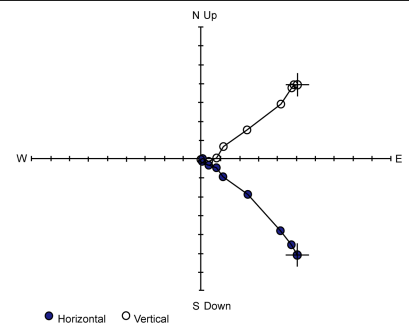
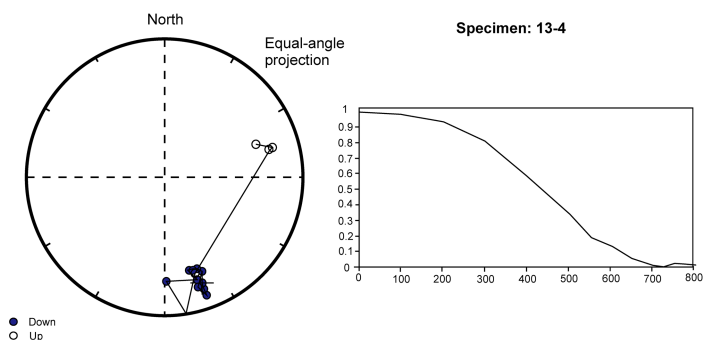
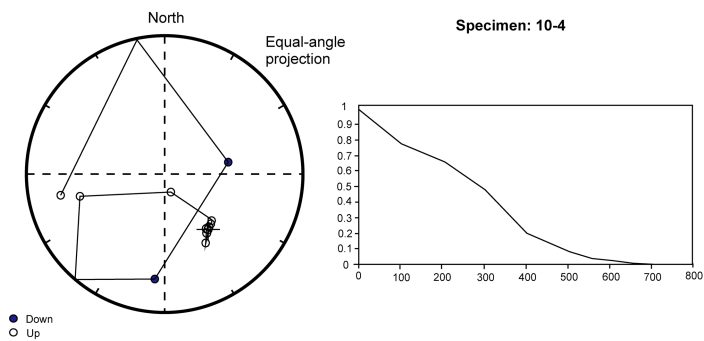
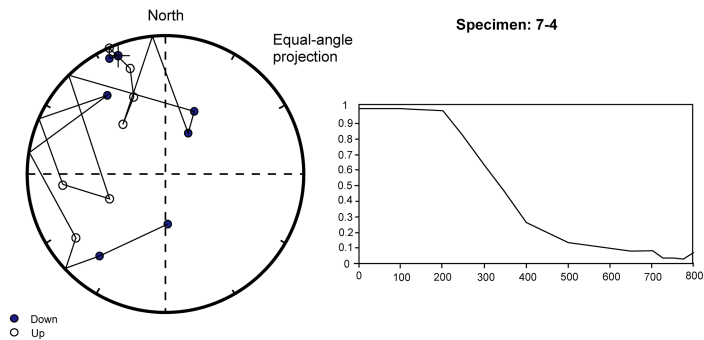
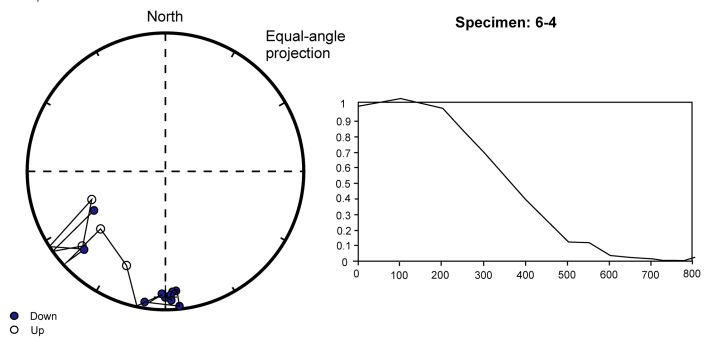
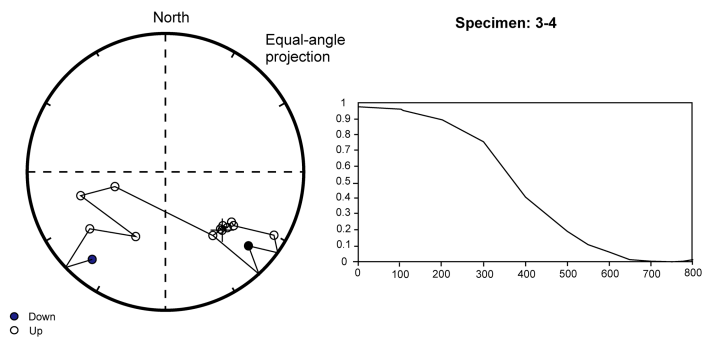




Extended Data Fig. 7 | See next page for caption.

**Extended Data Fig. 7 | Stepwise AF-demagnetization diagrams and vector end-point diagrams.** Data is provided for five representative subsamples (denoted specimens) from the Calio excavation site and the road section further east. The analysed specimens were taken from palaeomagnetic block samples Sp1, Sp2, Sp6, Sp7 and Sp9. The first sample number indicates the block sample number, whereas the second number refers to subsamples

obtained from the block samples (e.g., Specimen 6-1 is the first subsample obtained from palaeomagnetic block sample Sp6). Open circles on the orthogonal projection indicate the vertical component of magnetization and the solid circles the horizontal component. Open circles on the equal area projection diagram indicate an upper hemisphere magnetic direction. Solid circles indicate a lower hemisphere magnetic direction.

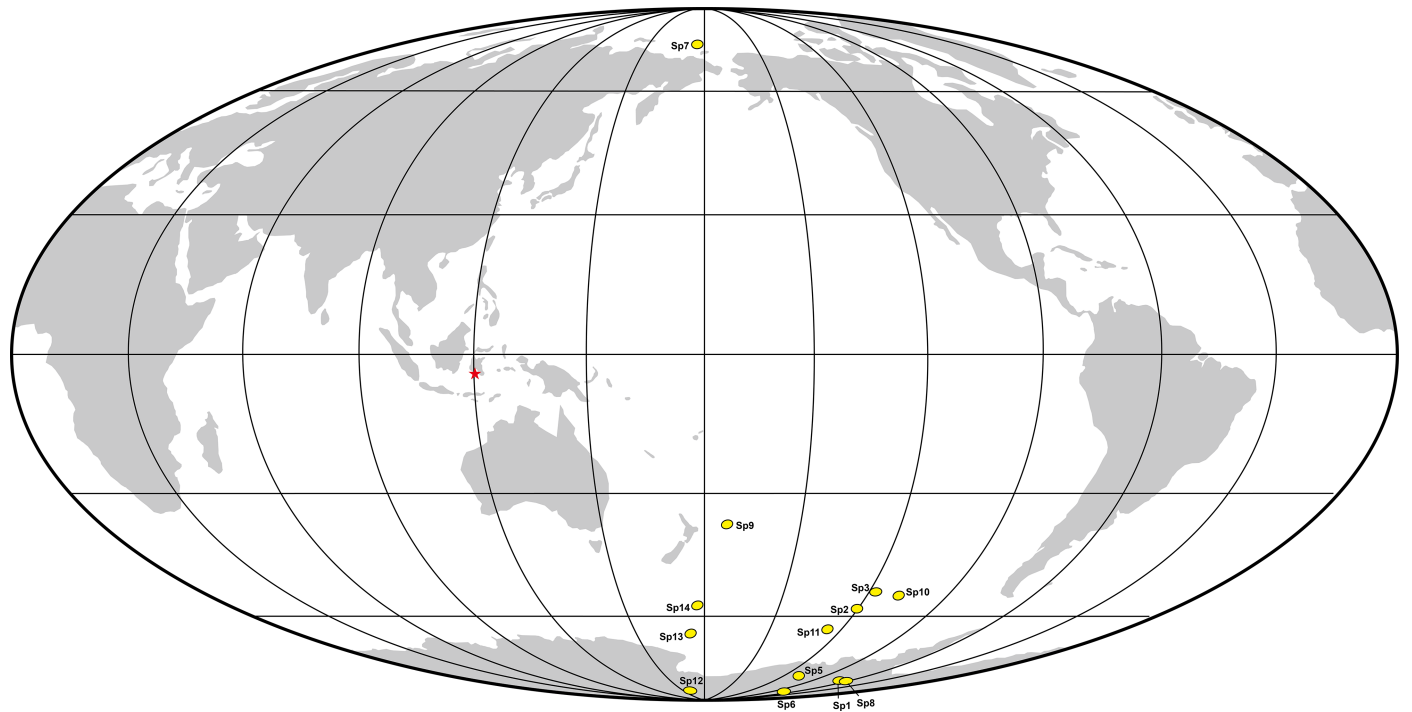


Extended Data Fig. 8 | See next page for caption.

**Extended Data Fig. 8 | Stepwise Thermal demagnetization (TD) diagrams and vector end-point diagrams.** Data is provided for five representative samples from the Calio excavation site and the road section further east. TD-analyzed subsamples (denoted “Specimens”) were taken from palaeomagnetic block samples Sp3, Sp6, Sp7, Sp10, and Sp13 (e.g., Specimen 3-4 denotes

subsample 4 from block sample Sp3). Open circles on the orthogonal projection indicate the vertical component of magnetization and the solid circles the horizontal component. Open circles on the equal area projection diagram indicate an upper hemisphere magnetic direction. Solid circles indicate a lower hemisphere magnetic direction.





**Extended Data Fig. 9 | Virtual Geomagnetic Pole (VGP) plots.** Data is provided for all palaeomagnetism samples from the Calio excavation site and other samples taken along the stratigraphic section. Yellow circles represent the VGP with sample numbers. The red star represents the sample site location.

Extended Data Table 1 | ChRMs comparison of alternating field (AFD) and thermal demagnetization (TD) treatment

Sample-specimen number	Stratigraphy	Number of subsamples ("Specimens")	ChRM Isolation Field (mT)	Mean declination using Alternating Field	Mean inclination using Alternating field	ChRM Isolation Temperature (°C)	Declination using Thermal	Inclination using Thermal	Mean Angular Deviation (Thermal)
Sp3-4	Calio excavation; Beru Member B	3	10-40	158.1	-26.9	200-600	132.4	-28.3	3.5
Sp6-4	Beru Member A	3	10-40	176.1	1.9	200-600	177.3	7.4	1.7
Sp7-4	Beru Member A	3	10-40	348.7	-22.8	300-600	340.3	-15.5	10.7
Sp8-4	Beru Member A	3	5-40	197.5	-14.6	300-775	118.5	-9.5	27.4
Sp10-4	Beru Member A	3	7.5-40	155.6	-32.6	200-600	143	-36.2	0.9
Sp13-4	Beru Member A	3	50-70	157.8	43.9	400-550	163.7	19.5	2

Extended Data Table 2 | Mean palaeomagnetic direction results of the sampled horizons

Sample number	Stratigraphy	Number of sub-samples	Mean declination	Mean inclination	Mean Maximum Angular Deviation	Fisher statistics				
						VGP latitude	VGP longitude	k	α95	Magnetic polarity*
Sp1	Calio excavation; Beru Member B	3	178.7	-11.8	12.1	-80.3	-67.7	65.09	11.5	R
Sp2	Calio excavation; Beru Member B	3	153.2	-22.1	5.3	-59.3	-120	73.97	10.8	R
Sp3	Calio excavation; Beru Member B	4	149.6	-27.9	2.9	-54.7	-117.7	33.19	21.7	R
Sp4	Beru excavation; Beru Member B	na	na	na	na	na	na	na	na	na
Sp5	Near Beru-Bulu Carulle excavation; Beru Member B	3	170.0	-8.8	3.4	-77.1	-111.1	107.69	11.9	R
Sp6	Beru Member A	4	178.2	-0.2	3	-85.8	-85.6	133.62	10.7	R
Sp7	Beru Member A	4	346.6	-24.6	8.7	74.5	177.2	72.9	14.5	N
Sp8	Beru Member A	4	179.4	-11.4	15.3	-80.6	-63.6	4.57	48.4	R
Sp9	Beru Member A	3	228.1	-28.2	5.7	-38.8	-172.6	2.66	99.4	I
Sp10	Beru Member A	4	151.7	-34.1	3.4	-54	-109.7	123.89	11.1	R
Sp11	Beru Member A	3	155.6	-12.6	3.2	-63.6	-127.6	307.27	27.7	R
Sp12	Beru Member A	3	181.4	3.2	6.3	-87.5	154.2	142.56	10.4	R
Sp13	Beru Member A	4	159.3	33.4	4.1	-65	172.7	41.58	19.4	R
Sp14	Samaoling Member	3	151.2	35.4	4.5	-57.7	178.2	625.33	4.9	R

A representative GPS location for the sampled trajectory is S4°20.112', E120°1.049. VGP = virtual geomagnetic pole; k = precision parameter; α95 = radius of 95% confidence circle; \*R = Reverse polarity; N = Normal polarity; I = Intermediate polarity; na = not available. Note that sample numbers are not in stratigraphic order.

**Extended Data Table 3 | Uranium series data (LA-MC-ICPMS) obtained from two *Celebochoerus* fossil teeth at Calio**

Sample	Dental tissues	U (ppm)	Error (2s)	U/Th	$^{234}\text{U}/^{238}\text{U}$	Error (2s)	$^{230}\text{Th}/^{238}\text{U}$	Error (2s)	Age	Error (2s)	$^{234}\text{U}/^{238}\text{U}$ initial	Error (2s)
Molar M <sup>3</sup>	enamel	0.7	0.1	4453	1.017	0.026	1.015	0.058			-	
	enamel	0.7	0.1	6173	1.045	0.037	0.736	0.066	131	12.2	1.065	0.053
	enamel	1.1	0.4	10477	1.086	0.037	0.723	0.091	117	17.6	1.120	0.058
	enamel	0.1	0	1416	1.076	0.083	1.211	0.160			-	
	EDJ	5.7	1.5	54003	1.043	0.022	0.705	0.048	121.4	9.5	1.061	0.032
	dentine	53.6	23.1	414980	1.159	0.030	0.819	0.054	128.1	8.4	1.228	0.048
	dentine	179.5	2.6	1338316	1.201	0.002	0.897	0.016	140.9	4.3	1.299	0.007
	dentine	168.0	4.6	1330864	1.205	0.002	0.897	0.028	139.9	7.8	1.304	0.010
	dentine	177.9	5.1	1406610	1.207	0.002	0.985	0.024	169.2	8.4	1.334	0.011
	dentine	175.0	4.9	1522031	1.206	0.002	0.991	0.019	171.9	6.2	1.335	0.009
	dentine	188.5	5.6	1506109	1.204	0.002	1.002	0.012	177.2	4.1	1.336	0.007
	dentine	189.3	8	1355150	1.202	0.002	0.988	0.026	172.3	9.4	1.329	0.012
	dentine	180.2	4	1371265	1.202	0.002	0.874	0.025	133.8	6.3	1.295	0.008
	dentine	172.1	2.3	650746	1.181	0.002	0.902	0.023	148	6.6	1.275	0.008
	dentine	195.5	7.8	5736	1.094	0.006	0.808	0.016	141.7	3.7	1.140	0.010
	<b>Average Enamel</b>	<b>0.7</b>	<b>0.17</b>	-	<b>1.056</b>	<b>0.046</b>	<b>0.921</b>	<b>0.094</b>			-	
	<b>Average Dentine</b>	<b>153.2</b>	<b>6.31</b>	-	<b>1.173</b>	<b>0.007</b>	<b>0.897</b>	<b>0.026</b>			-	
Premolar P <sup>4</sup>	enamel	0.1	0.3	918748	1.026	0.144	0.983	0.239	325.3	227.2	1.066	0.749
	enamel	0.2	0.1	1311734	1.003	0.095	0.937	0.137	294.5	66.1	1.007	0.429
	enamel	0.3	0.2	7224011	1.012	0.067	0.938	0.104	279.9	63.9	1.027	0.294
	enamel	0.3	0.1	108888250	1.106	0.069	0.948	0.121	198.7	55.3	1.186	0.266
	EDJ	3.4	10.2	2273317	1.072	0.137	1.062	0.212	372.6	176.3	1.207	0.871
	EDJ	26.4	20.8	34936984	1.013	0.024	1.061	0.040			-	
	dentine	38.6	6.0	2571158	1.035	0.018	0.974	0.045	293.0	67.0	1.079	0.096
	dentine	39.8	10.7	2129	1.062	0.013	0.936	0.014	221.8	0.3	1.115	0.048
	dentine	69.7	34.1	4465	1.085	0.008	0.873	0.015	171.1	6.6	1.137	0.028
	dentine	122.5	36.0	4786	1.162	0.016	1.001	0.045	196.0	28.7	1.281	0.077
	dentine	114.8	18.4	53564	1.170	0.009	1.016	0.013	199.7	3.8	1.299	0.034
	dentine	62.4	28.3	802353	1.082	0.017	0.915	0.018	193.8	0.7	1.142	0.058
	dentine	59.1	16.4	357950	1.071	0.008	0.890	0.014	186.2	6.3	1.121	0.029
	<b>Average Enamel</b>	<b>0.3</b>	<b>0.11</b>	-	<b>1.040</b>	<b>0.103</b>	<b>0.951</b>	<b>0.151</b>			-	
	<b>Average Dentine</b>	<b>72.4</b>	<b>21.4</b>	-	<b>1.095</b>	<b>0.013</b>	<b>0.944</b>	<b>0.023</b>			-	

Uranium series data was obtained on the faunal remains using a laser ablation Multicollector Inductively Coupled Plasma Mass Spectrometer (LA-MC-ICPMS) on the sectioned teeth. EDJ stands for enamel-dentine junction and represents the zone in-between both dental tissues that usually behaves differently for uranium diffusion than the bulk of enamel and dentine. The first EDJ measurement for each tooth relates to early enamel prisms, while the second measurements correspond to the upper dentine tissues in contact with the enamel crystals. The average reported at the bottom of each table section is calculated for each dental tissue (enamel and dentine), with the associated mean error. Empty cells represent values that either cannot be calculated or the resulting age calculation is irrelevant (i.e., age of the average value for dentine).



Extended Data Table 4 | US-ESR dating data parameters summary used for the age modelling (1 sigma error)

Sample	Molar M <sup>3</sup>	Premolar P <sup>4</sup>
Enamel		
Dose (Gy) <sup>a</sup>	2116 ± 118	2267 ± 99
U (ppm) <sup>b</sup>	0.66 ± 0.09	0.31 ± 0.06
<sup>234</sup> U/ <sup>238</sup> U <sup>b</sup>	1.056 ± 0.0024	1.040 ± 0.063
<sup>230</sup> Th/ <sup>234</sup> U <sup>b</sup>	0.873 ± 0.07	0.919 ± 0.05**
Initial thickness (µm)	1125 ± 45	1010 ± 110
Removed thickness (µm) <sup>#</sup>	100 ± 15	100 ± 15
Water (%)	3 ± 3	3 ± 3
Dentine		
U (ppm) <sup>b</sup>	153 ± 3.4	72.4 ± 12.6
<sup>234</sup> U/ <sup>238</sup> U <sup>b</sup>	1.173 ± 0.004	1.095 ± 0.008
<sup>230</sup> Th/ <sup>234</sup> U <sup>b</sup>	0.779 ± 0.030	0.862 ± 0.019
Water (%)	5 ± 5	5 ± 5
Sediment		
U (ppm) <sup>b</sup>	2.52 ± 0.57	2.52 ± 0.57
Th (ppm) <sup>b</sup>	4.86 ± 0.27	4.86 ± 0.27
K (%) <sup>b</sup>	1.78 ± 0.07	1.78 ± 0.07
Water (%)	15 ± 15	15 ± 15
External dose rate sediment		
Beta dose (µGy a <sup>-1</sup> )	162 ± 28	182 ± 35
Gamma dose (µGy a <sup>-1</sup> )	791 ± 144	791 ± 144
Cosmic (µGy a <sup>-1</sup> )	213 ± 19	213 ± 19
Combined US-ESR ages		
Internal dose rate (µGy a <sup>-1</sup> ) <sup>d</sup>	95 ± 44	57 ± 31
Beta dose dentine (µGy a <sup>-1</sup> ) <sup>d</sup>	499 ± 229	345 ± 187
P enamel <sup>d</sup>	0.69 ± 0.27	0.11 ± 0.17
P dentine <sup>d</sup>	1.98 ± 0.46	1.02 ± 0.30
Total dose rate (µGy a <sup>-1</sup> ) <sup>d</sup>	1760 ± 276	1588 ± 241
CSUS-ESR age (ka) <sup>c</sup>	1547 ± 246	1733 ± 367
US-ESR age (ka) <sup>c</sup>	1140 +155/-273	1368 +207/-306
US-ESR age (ka) <sup>d</sup>	1202 ± 176	1428 ± 208

ESR dose equivalent measurements were conducted on powder for the molar (M<sup>3</sup>) sample and on the fragment for the premolar (P<sup>4</sup>).

<sup>a</sup>Dose equivalent De obtained using MCDoseE 2.0, with SSE (from ref. 47).

<sup>b</sup>Concentrations and ratio values were obtained by both LA-MC-ICPMS and (corrected by LA-ICPMS for concentrations) on both teeth and dental tissues. Sediment content was obtained by ICPMS solution only.

<sup>c</sup>The age was calculated using the Grün<sup>51</sup> DATA program and <sup>d</sup>US-ESR matlab® algorithm from Shao et al.<sup>50</sup>, with the dose rate conversion factors of Guérin et al.<sup>49</sup>, and the enamel and dentine density of 2.95 and 2.85 respectively from Grün<sup>63</sup>.

<sup>d</sup>Close System U-series (CSUS) refers to ref. 64. It is a US-ESR age calculated under the assumption that present-day uranium in a sample was accumulated at the apparent U-series age within a short time span. The measured uranium contents in dentine and enamel of the teeth are therefore used to calculate the total dose during the apparent U-series ages and represent the extreme case, making the age calculated to be a maximum age. DATA was used to estimate the external dose rate contribution using the sediment content.

**\*\***The enamel <sup>230</sup>Th/<sup>234</sup>U and <sup>234</sup>U/<sup>238</sup>U associated error for the premolar sample could not be used for the US-ESR calculation using Shao et al.<sup>50</sup>. Instead, the associated errors had to be reduced to 0.05 (rather than 0.096) to allow for the model to run. The overall impact on the age calculation and associated error is insignificant compared to other uncertainties and is estimated to be less than 10 ka.

<sup>#</sup>The 100 µm of enamel was removed on both sides.

ESR dose equivalent measurements were conducted on powder for the molar (M<sup>3</sup>) sample and on the fragment for the premolar (P<sup>4</sup>).

## Reporting Summary

Nature Portfolio wishes to improve the reproducibility of the work that we publish. This form provides structure for consistency and transparency in reporting. For further information on Nature Portfolio policies, see our [Editorial Policies](#) and the [Editorial Policy Checklist](#).

### Statistics

For all statistical analyses, confirm that the following items are present in the figure legend, table legend, main text, or Methods section.

n/a Confirmed

- ☐ ☒ The exact sample size ( $n$ ) for each experimental group/condition, given as a discrete number and unit of measurement
- ☐ ☒ A statement on whether measurements were taken from distinct samples or whether the same sample was measured repeatedly
- ☐ ☒ The statistical test(s) used AND whether they are one- or two-sided  
*Only common tests should be described solely by name; describe more complex techniques in the Methods section.*
- ☒ ☐ A description of all covariates tested
- ☐ ☒ A description of any assumptions or corrections, such as tests of normality and adjustment for multiple comparisons
- ☐ ☒ A full description of the statistical parameters including central tendency (e.g. means) or other basic estimates (e.g. regression coefficient) AND variation (e.g. standard deviation) or associated estimates of uncertainty (e.g. confidence intervals)
- ☐ ☒ For null hypothesis testing, the test statistic (e.g.  $F$ ,  $t$ ,  $r$ ) with confidence intervals, effect sizes, degrees of freedom and  $P$  value noted  
*Give  $P$  values as exact values whenever suitable.*
- ☒ ☐ For Bayesian analysis, information on the choice of priors and Markov chain Monte Carlo settings
- ☒ ☐ For hierarchical and complex designs, identification of the appropriate level for tests and full reporting of outcomes
- ☒ ☐ Estimates of effect sizes (e.g. Cohen's  $d$ , Pearson's  $r$ ), indicating how they were calculated

Our web collection on [statistics for biologists](#) contains articles on many of the points above.

### Software and code

Policy information about [availability of computer code](#)

Data collection

n/a

Data analysis

Software programs used for Uranium-series/Electron Spin Resonance dating: IsoPlotR, UThwigl, McDoseE 2.0, Matlab, DATA program, lolite. Software programs used for palaeomagnetic dating: PuffinPlot, IAPD 2000. No software was used for collection of primary field data.

For manuscripts utilizing custom algorithms or software that are central to the research but not yet described in published literature, software must be made available to editors and reviewers. We strongly encourage code deposition in a community repository (e.g. GitHub). See the Nature Portfolio [guidelines for submitting code & software](#) for further information.

### Data

Policy information about [availability of data](#)

All manuscripts must include a [data availability statement](#). This statement should provide the following information, where applicable:

- Accession codes, unique identifiers, or web links for publicly available datasets
- A description of any restrictions on data availability
- For clinical datasets or third party data, please ensure that the statement adheres to our [policy](#)

The data supporting the findings of this study are provided in the Supplementary Information. Raw and additional Source data are available from publicly available Zenodo data repositories. Access to primary archaeological assemblages (e.g., stone artefacts, fossil fauna) is available to researchers upon reasonable request.

## Research involving human participants, their data, or biological material

Policy information about studies with [human participants or human data](#). See also policy information about [sex, gender \(identity/presentation\), and sexual orientation](#) and [race, ethnicity and racism](#).

Reporting on sex and gender	n/a
Reporting on race, ethnicity, or other socially relevant groupings	n/a
Population characteristics	n/a
Recruitment	n/a
Ethics oversight	n/a

Note that full information on the approval of the study protocol must also be provided in the manuscript.

## Field-specific reporting

Please select the one below that is the best fit for your research. If you are not sure, read the appropriate sections before making your selection.

☒ Life sciences ☐ Behavioural & social sciences ☐ Ecological, evolutionary & environmental sciences

For a reference copy of the document with all sections, see [nature.com/documents/nr-reporting-summary-flat.pdf](https://www.nature.com/documents/nr-reporting-summary-flat.pdf)

## Life sciences study design

All studies must disclose on these points even when the disclosure is negative.

Sample size	The study comprised an archaeological excavation of Early Pleistocene fluvial sandstone deposits (Beru Member Sub-Unit B) at an open site (Calio) in the Walanae Depression of South Sulawesi, Indonesia. Systematic excavations were carried out at Calio in 2019 and 2021–2022, targeting an area on an ENE-WSW trending ridge. In 2019, we opened a total of six contiguous 1 m <sup>2</sup> excavation units (denoted squares B1U1 to B1U6) using arbitrary 10-cm thick intervals (spits). The first square, B1U1, was initiated at the find site of Artefact 1. An additional nine one-metre square units (B2U1, B2U2, B2U3, B3U1, B3U2, B3U3, B4U1, B4U2 and B4U3) were placed on the west side of the previously excavated units in 2021–2022. The research sample consisted of a primary archaeological dataset (stone artefacts) recovered during the excavations. Sediment samples were also taken for palaeomagnetic dating and a vertebrate fossil (maxilla of extinct suid <i>Celebochoerus</i> ) was collected for coupled Uranium-series/ESR dating. In the field, sample sizes were chosen based on available field conditions (e.g., visible fossil outcrop exposures) and time and budget constraints.
Data exclusions	There were no data exclusions.
Replication	It is possible that similar stone artefacts and fossil fauna findings will be recovered from future excavation of adjacent deposits. However, replication of primary field results is not strictly possible due to the nature of archaeological excavation, which destroys the sedimentary strata under excavation. Palaeomagnetic dating and U-series/ESR dating experiments can potentially be repeated on remaining samples.
Randomization	Not possible/relevant under primary field research conditions.
Blinding	Not possible/relevant under primary field research conditions.

## Reporting for specific materials, systems and methods

We require information from authors about some types of materials, experimental systems and methods used in many studies. Here, indicate whether each material, system or method listed is relevant to your study. If you are not sure if a list item applies to your research, read the appropriate section before selecting a response.

### Materials & experimental systems

n/a	Involved in the study
<input checked="" type="checkbox"/>	<input type="checkbox"/> Antibodies
<input checked="" type="checkbox"/>	<input type="checkbox"/> Eukaryotic cell lines
<input checked="" type="checkbox"/>	<input type="checkbox"/> Palaeontology and archaeology
<input checked="" type="checkbox"/>	<input type="checkbox"/> Animals and other organisms
<input checked="" type="checkbox"/>	<input type="checkbox"/> Clinical data
<input checked="" type="checkbox"/>	<input type="checkbox"/> Dual use research of concern
<input checked="" type="checkbox"/>	<input type="checkbox"/> Plants

### Methods

n/a	Involved in the study
<input checked="" type="checkbox"/>	<input type="checkbox"/> ChIP-seq
<input checked="" type="checkbox"/>	<input type="checkbox"/> Flow cytometry
<input checked="" type="checkbox"/>	<input type="checkbox"/> MRI-based neuroimaging



Plants

Seed stocks	n/a
Novel plant genotypes	n/a
Authentication	n/a